

GAIN OPTIMIZATION FOR CASCADED INDI CONTROL WITH INTEGRATED PERFORMANCE AND ROBUSTNESS REQUIREMENTS

Denis Surmann[1] & Stephan Myschik[1]

[1]Institute for Aeronautical Engineering, University of the Bundeswehr Munich, Werner-Heisenberg-Weg 39, Neubiberg, 85577, Bavaria, Germany

Abstract

This paper presents a gain-optimization framework for cascaded sensor-based incremental nonlinear dynamic inversion (INDI) flight control of a fixed-wing electric vertical-take-off-and-landing (eVTOL) aircraft. The closed-loop performance remains strongly dependent on tunable gains, which are often selected manually and insufficiently documented in the literature. The method reformulates the gain-tuning task as a constrained multi-objective optimization problem, in which tracking, disturbance rejection, practical achievability, and disk-margin robustness requirements are evaluated on a linear closed-loop model. Particle swarm optimization (PSO) is used to determine the inner- and outer-loop error-controller gains. The optimized controller is assessed in hover flight using frequency- and time-domain analyses, including aerodynamic, propulsion, mass-property, and delay variations. The results show that the optimized gains satisfy the prescribed performance and robustness requirements. A nonlinear hover simulation with sensor effects and delays further confirms the tracking performance of the tuned inner loop.

Keywords: Incremental nonlinear dynamic inversion; Gain optimization; Control performance and robustness

Nomenclature

$\mathbf{A}_{ineq}$	Linear inequality constraints matrix
$\mathbf{b}_{ineq}$	Linear inequality constraints vector
$\vec{\boldsymbol{d}}$	Disturbance vector
$\vec{\boldsymbol{F}}$	Force vector
$f_i(\mathbf{p})$	Soft-objective cost function
g	Gravitational acceleration
$g_j(\mathbf{p})$	Hard-constraint cost function
$J(\mathbf{p})$	Generalized cost function
$\mathbf{K}_P$	Gain matrix
$L_{yu}(s)$	Open-loop transfer function with input u and output y
m	Aircraft mass
$\vec{\boldsymbol{M}}$	Moment vector
$\mathbf{p}$	Tunable parameter vector
$\vec{\boldsymbol{r}}$	Position vector $[x,y,z]^T$
$S_{yu}(s)$	Sensitivity with input u and output y
$T_{yu}(s)$	Closed-loop transfer function with input u and output y
$T_{ref}(s)$	Reference-model transfer function
$\mathbf{u}$	Input vector
$\mathbf{B}_v$	Control effectiveness matrix
$\vec{\boldsymbol{V}}$	Velocity vector $[u,v,w]^T$
V_A	Airspeed
$\vec{\dot{\boldsymbol{V}}}$	Acceleration vector $[\dot{u},\dot{v},\dot{w}]^T$
$W_e(s)$	Error weighting function
w_i	Weighting factor of $f_i(\mathbf{p})$
$\mathbf{x}$	State vector
$\dot{\mathbf{x}}$	State derivative vector
$\mathbf{y}$	Output vector
α	Angle of attack
β	Sideslip angle
ε_{DR}	Relative tolerance band for disturbance rejection
Φ	Bank angle
$\boldsymbol{\nu}$	Pseudo-control vector
ρ	Air density
$\overline{\sigma}(\cdot)$	Maximum singular value
τ_{DR}	Decay time constant of the disturbance-rejection error bound
Θ	Pitch angle
ω_{ce}	Crossover frequency of the error weighting
$\vec{\boldsymbol{\omega}}$	Angular velocity vector
$\vec{\dot{\boldsymbol{\omega}}}$	Angular acceleration vector
$\boldsymbol{\xi}$	Reference state vector
Ψ	Yaw angle

Frames

A	Aerodynamic frame
B	Body-fixed frame
C	Control frame
E	Earth-centered-Earth-fixed frame
I	Inertial frame
N	Navigation frame
O	North-East-Down frame

1 Introduction

Flight control systems are essential for the safe and reliable operation of manned and unmanned aircraft. In recent years, electric vertical-take-off-and-landing vehicles (eVTOLs) have received increasing attention due to their potential use in urban and regional air mobility. Fixed-wing eVTOL configurations are particularly attractive because they combine vertical take-off and landing capability with efficient wingborne flight. However, this configuration also introduces a challenging transition phase, during which aerodynamic forces, propulsive forces, and actuator effectiveness change significantly. Different control concepts have therefore been proposed to handle specific parts of the flight envelope [1]. In contrast, nonlinear control approaches based on incremental nonlinear dynamic inversion (INDI) have been applied to provide a unified control formulation across hover, transition, and wingborne flight [2, 3, 4].

A major advantage of INDI is its incremental formulation. Instead of relying on a complete model inversion of the nonlinear aircraft dynamics, the control input is computed from increments around the current operating condition. In sensor-based INDI, measured or estimated accelerations are used to represent the current system response, while the model dependency is mainly shifted to the local control effectiveness matrix. This is particularly beneficial for eVTOLs, where the aerodynamic and propulsive interactions are strongly nonlinear and difficult to model accurately over the full flight envelope. The sensor-based formulation can therefore reduce the dependency on a complete onboard model and improve the compensation of disturbances and model mismatch [5, 6, 7, 8]. At the same time, this approach introduces specific implementation challenges. Since the controller relies on measured or estimated derivatives and actuator states, its performance can be affected by sensor noise, filtering, signal delays, and synchronization errors [9].

Regardless of the selected control architecture, the closed-loop behavior depends strongly on tunable parameters, commonly referred to as controller gains. In many flight-control applications, the derivation of these gains is only partially documented, which suggests that manual tuning is still frequently used. This process can be time-consuming and difficult to reproduce [10]. Consequently, structured multi-objective gain-design methods have been investigated for aircraft and eVTOL control applications [11, 12, 13, 14]. For INDI-based control, recent surveys emphasize that gain-design methods have received comparatively limited attention, despite their importance for practical controller implementation [6, 7].

This paper addresses this gap by presenting a gain-optimization framework for a cascaded sensor-based INDI controller. The work builds on previous gain-design studies in which MATLAB® `systune` was used for tuning [11, 15]. While such tools provide an efficient way to tune controllers against multiple requirements, the resulting workflow can be difficult to customize when user-defined cost functions, requirement formulations, or post-optimization analyses are required. Therefore, the tuning problem is reformulated in this work as an explicit constrained optimization problem and solved using particle swarm optimization (PSO). The proposed formulation allows for tracking, disturbance rejection, practical achievability, inequality constraints, and disk-margin requirements to be expressed directly and evaluated in a common framework.

In contrast to approaches that include nonlinear simulations directly in the optimization process [12], the proposed method performs gain optimization on a linearized closed-loop representation of the aircraft and controller. Tracking and disturbance-rejection objectives are evaluated in the frequency domain, while robustness is enforced using disk-margin requirements at selected loop-breaking points. This reduces computational effort and allows the user to inspect the achieved performance over the relevant frequency range. After the nominal optimization, the optimized gains are further assessed using post-optimization linear analyses with aerodynamic, propulsion, mass-property, and delay variations, followed by nonlinear simulations of the resulting controller.

The remainder of this paper is structured as follows. Section 2 introduces the nonlinear aircraft simulation model, including the considered fixed-wing eVTOL configuration, actuator dynamics, flight-dynamic model, trimming, and linearization. Section 3 describes the cascaded sensor-based INDI flight-control architecture and the error-controller gains used as tuning parameters. Section 4 presents the linear optimization environment, the constrained optimization problem, and the PSO-based strategy. Section 5 defines the closed-loop and open-loop requirements used for gain optimization and

explains the post-optimization linear assessment. Section 6 presents the linear and nonlinear results, including tracking, disturbance rejection, disk-margin evaluation, delay analysis, and nonlinear hover simulation. Finally, Section 7 summarizes the main findings and outlines future work.

2 Aircraft Simulation Model

This section introduces the nonlinear aircraft simulation model used as the basis for trimming, linearization, and gain optimization. The considered aircraft is the conceptual fixed-wing eVTOL demonstrator *PEGASUS*, shown in Fig. 1. The vehicle combines conventional wingborne flight capability with vertical take-off and landing functionality through tiltable propulsion units.

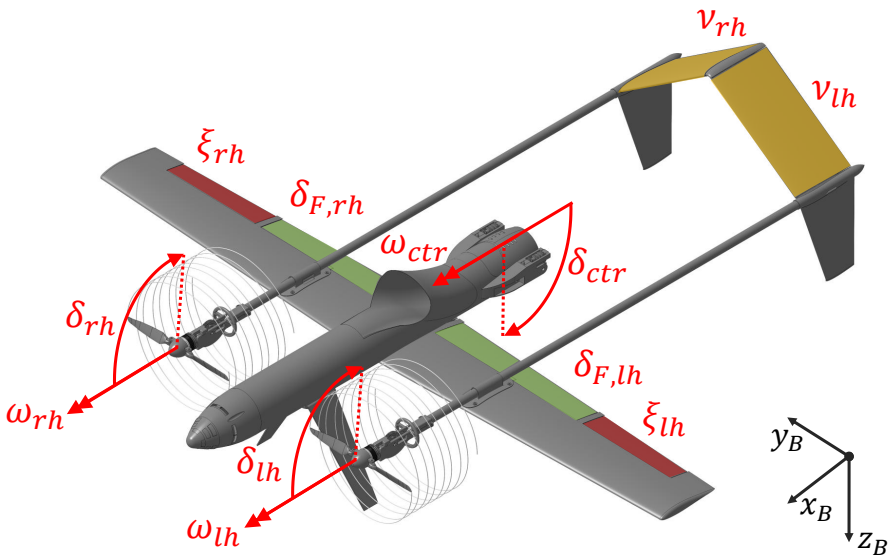


Figure 1 – Configuration and control effectors of the fixed-wing eVTOL demonstrator *PEGASUS*.

2.1 Aircraft Configuration and Control Effectors

The aircraft has a fixed-wing configuration and a take-off mass of approximately $11\ kg$, including payload. Vertical take-off and landing capability is provided by a propulsion system consisting of two wing-mounted tilt propellers and one central impeller. The thrust generated by the propellers is adjusted by their rotational speeds ω_{lh} and ω_{rh}, while the thrust direction is controlled through the corresponding tilt angles δ_{lh} and δ_{rh}. The central impeller can be rotated by the tilt angle δ_{ctr}.
During hover flight, the central impeller and the two propellers predominantly provide upward thrust at $\delta_{ctr} = 90°$ and $\delta_{lh} = \delta_{rh} = 90°$. Yaw control in hover is generated by differential tilt deflections of the two propellers, whose maximum tilt angle is $105°$.
During transition, the propulsion units are gradually tilted forward to generate horizontal acceleration. At the same time, the aircraft maintains a positive pitch attitude in order to preserve a positive angle of attack and thus generate aerodynamic lift. This flight regime is characterized by strongly varying control effectiveness, as aerodynamic surfaces, propulsion tilt angles, and thrust magnitudes simultaneously contribute to force and moment generation.
Once the aircraft exceeds its aerodynamic stall speed of approximately $15\ m/s$, the main lift contribution is generated by the wing, and the vehicle behaves similarly to a conventional fixed-wing aircraft. In this wingborne regime, moments are primarily generated by aerodynamic control surfaces, namely the ailerons ξ, the ruddervators ν, and the flaps δ_F, to provide additional lift and drag forces.

2.2 Nonlinear Simulation Framework

The nonlinear simulation framework consists of actuator dynamics, the nonlinear flight dynamic model (FDM), and a sensor model representing the measurement signals available to the flight control system. The simulation model can be initialized externally, allowing the aircraft states and operating conditions to be prescribed for trimming, linearization, and closed-loop simulation studies.

The control effectors are grouped into propulsion units, propulsion tilt mechanisms, and aerodynamic surfaces. The propulsion dynamics are approximated by first-order systems, which capture the dominant thrust build-up behavior. The tilt mechanisms and aerodynamic control surfaces are modeled as second-order systems in order to account for inertia and damping effects [16, 17]. Each actuator is modeled independently, enabling the simulation of redundant control allocation and actuator-specific limitations.

2.3 Flight Dynamic Model

The core of the simulation framework is the nonlinear FDM. The aircraft dynamics are represented by a rigid-body degree-of-freedom (DoF) formulation with an arbitrary aircraft reference point R. The translational and rotational equations of motion are given by [16, 18]

$$\begin{aligned}\left(\dot{\vec{V}}_K^R\right)_B^{EB} = &\frac{\left(\vec{F}_T^R\right)_B}{m} - \left(\vec{\omega}_K^{EB}\right)_B \times \left(\vec{V}_K^R\right)_B^E - 2\left(\vec{\omega}_K^{IE}\right)_B \times \left(\vec{V}_K^R\right)_B^E \\ &- \left(\vec{\omega}_K^{IE}\right)_B \times \left(\left(\vec{\omega}_K^{IE}\right)_B \times \left(\vec{r}^R\right)_B\right) \\ &- \left(\dot{\vec{\omega}}_K^{IB}\right)_B^B \times \left(\vec{r}^{RG}\right)_B - \left(\vec{\omega}_K^{IB}\right)_B \times \left(\left(\vec{\omega}_K^{IB}\right)_B \times \left(\vec{r}^{RG}\right)_B\right),\end{aligned} \tag{1}$$

$$\begin{aligned}\left(\dot{\vec{\omega}}_K^{IB}\right)_B^B = \left(I^R\right)_{BB}^{-1} \Bigg(&\left(\vec{M}_T^R\right)_B - \left(\vec{\omega}_K^{IB}\right)_B \times \left(\left(I^R\right)_{BB}\left(\vec{\omega}_K^{IB}\right)_B\right) \\ &- m\left(\vec{r}^{RG}\right)_B \times \left(\left(\dot{\vec{V}}_K^R\right)_B^{IB} + \left(\vec{\omega}_K^{IB}\right)_B \times \left(\vec{V}_K^R\right)_B^I\right)\Bigg).\end{aligned} \tag{2}$$

The kinematics of the attitude are described by

$$\begin{bmatrix}\dot{\Phi}\\ \dot{\Theta}\\ \dot{\Psi}\end{bmatrix} = \begin{bmatrix}1 & \sin\Phi\tan\Theta & \cos\Phi\tan\Theta\\ 0 & \cos\Phi & -\sin\Phi\\ 0 & \dfrac{\sin\Phi}{\cos\Theta} & \dfrac{\cos\Phi}{\cos\Theta}\end{bmatrix}\begin{bmatrix}p\\ q\\ r\end{bmatrix}. \tag{3}$$

The position propagation in the local navigation frame is obtained from the translational velocity of the aircraft reference point,

$$\begin{bmatrix}\dot{x}\\ \dot{y}\\ \dot{z}\end{bmatrix}_N = \mathbf{M}_{NO}\mathbf{M}_{OB}\begin{bmatrix}u_K^R\\ v_K^R\\ w_K^R\end{bmatrix}_B. \tag{4}$$

The total forces and moments acting at the aircraft reference point are composed of aerodynamic, propulsive, and gravitational contributions:

$$\left(\vec{F}_T^R\right)_B = \left(\vec{F}_A^R\right)_B + \left(\vec{F}_P^R\right)_B + \left(\vec{F}_G^R\right)_B, \tag{5}$$

$$\left(\vec{M}_T^R\right)_B = \left(\vec{M}_A^R\right)_B + \left(\vec{M}_P^R\right)_B + \left(\vec{M}_G^R\right)_B. \tag{6}$$

The aerodynamic model distinguishes between wingborne and hover-related aerodynamic effects. In wingborne flight, the aerodynamic forces are expressed in the aerodynamic frame as

$$\left(\vec{F}_{A,wb}^A\right)_A = \begin{bmatrix}-D\\ Q\\ -L\end{bmatrix}_A = \frac{1}{2}\rho V_A^2 S\begin{bmatrix}-C_D\\ C_Q\\ -C_L\end{bmatrix}_A, \tag{7}$$

and are transformed into the body-fixed frame according to

$$\left(\vec{F}_{A,wb}^A\right)_B = \mathbf{M}_{BA}\left(\vec{F}_{A,wb}^A\right)_A. \tag{8}$$

Here, L denotes lift, D drag, and Q the side force. Furthermore, ρ is the air density, V_A the airspeed, and S the wing reference area. The aerodynamic coefficients are modeled as functions of the aerodynamic states and control surface deflections. In compact form, the force coefficients are written as

$$C_D = C_{D0} + C_{Dq} q_A^* + C_{D\alpha} \alpha_A + C_{Du} \left(\xi_{lh}, \xi_{rh}, \nu_{lh}, \nu_{rh}, \delta_{F,lh}, \delta_{F,rh}\right), \tag{9}$$

$$C_Q = C_{Qp} p_A^* + C_{Qr} r_A^* + C_{Q\beta} \beta_A + C_{Qu} \left(\xi_{lh}, \xi_{rh}, \nu_{lh}, \nu_{rh}, \delta_{F,lh}, \delta_{F,rh}\right), \tag{10}$$

$$C_L = C_{L0} + C_{Lq} q_A^* + C_{L\alpha} \alpha_A + C_{Lu} \left(\xi_{lh}, \xi_{rh}, \nu_{lh}, \nu_{rh}, \delta_{F,lh}, \delta_{F,rh}\right). \tag{11}$$

The dynamic derivatives, also referred to as damping derivatives, are introduced using the dimensionless normalized angular rates

$$\begin{aligned} p_A^* &= \frac{b}{2V_A} p_A \\ q_A^* &= \frac{\bar{c}}{2V_A} q_A \\ r_A^* &= \frac{b}{2V_A} r_A, \end{aligned} \tag{12}$$

where b denotes the wingspan and $\bar{c}$ denotes the mean aerodynamic chord [16]. These quantities are referred to as normalized angular rates. The corresponding aerodynamic moments are formulated as

$$\left(\vec{\boldsymbol{M}}_{A,wb}^{A}\right)_B = \frac{1}{2}\rho V_A^2 S \begin{bmatrix} sC_l \\ \bar{c}C_m \\ sC_n \end{bmatrix}_B, \tag{13}$$

with the semi wingspan s. The moment contribution at the aircraft reference point is

$$\left(\vec{\boldsymbol{M}}_{A,wb}^{R}\right)_B = \left(\vec{\boldsymbol{M}}_{A,wb}^{A}\right)_B + \left(\vec{\boldsymbol{r}}^{RA}\right)_B \times \left(\vec{\boldsymbol{F}}_{A,wb}^{A}\right)_B. \tag{14}$$

For hover and low-speed flight, the wingborne aerodynamic formulation is not directly suitable, since the angle of attack becomes numerically unreliable as the airspeed approaches zero. Therefore, the low-speed aerodynamic contribution is approximated by an equivalent flat-plate (FP) model following [2]. The effective drag coefficients of each surface element i are obtained from

$$\begin{bmatrix} \tilde{C}_{FP_i,x} \\ \tilde{C}_{FP_i,y} \\ \tilde{C}_{FP_i,z} \end{bmatrix}_B = \begin{bmatrix} A_{x_i} & 0 & 0 \\ 0 & A_{y_i} & 0 \\ 0 & 0 & A_{z_i} \end{bmatrix}_B \begin{bmatrix} C_{FP_i,x} \\ C_{FP_i,y} \\ C_{FP_i,z} \end{bmatrix}_B, \tag{15}$$

where A_{x_i}, A_{y_i}, and A_{z_i} are the projected areas of the corresponding body element. The resulting aerodynamic force contribution of each element is

$$\left(\vec{\boldsymbol{F}}_{A,ho}^{R_{FP_i}}\right)_B = \frac{1}{2}\rho \left(\left| \left(\vec{\boldsymbol{V}}_A^{FP_i}\right)_B^E \right| \odot \left(\vec{\boldsymbol{V}}_A^{FP_i}\right)_B^E \right) \odot \begin{bmatrix} -\tilde{C}_{FP_i,x} \\ -\tilde{C}_{FP_i,y} \\ -\tilde{C}_{FP_i,z} \end{bmatrix}_B. \tag{16}$$

The aerodynamic velocity at the pressure point FP_i is computed from the velocity at the aircraft reference point and the rotational contribution,

$$\left(\vec{\boldsymbol{V}}_A^{FP_i}\right)_B^E = \left(\vec{\boldsymbol{V}}_A^{R}\right)_B^E + \left(\vec{\boldsymbol{\omega}}_K^{OB}\right)_B \times \left(\vec{\boldsymbol{r}}^{RFP_i}\right)_B, \tag{17}$$

with

$$\left(\vec{\boldsymbol{V}}_A^{R}\right)_B^E = \left(\vec{\boldsymbol{V}}_K^{R}\right)_B^E - \left(\vec{\boldsymbol{V}}_W^{R}\right)_B^E. \tag{18}$$

The corresponding moment contribution of each body element is

$$\left(\vec{\boldsymbol{M}}_{A,ho}^{R_{FP_i}}\right)_B = \left(\vec{\boldsymbol{r}}^{RFP_i}\right)_B \times \left(\vec{\boldsymbol{F}}_{A,ho}^{R_{FP_i}}\right)_B. \tag{19}$$

The total hover-related aerodynamic forces and moments are obtained by summing over all considered body elements:

$$\left(\vec{\boldsymbol{F}}_{A,ho}^{R}\right)_B = \sum_i \left(\vec{\boldsymbol{F}}_{A,ho}^{R_{FP_i}}\right)_B, \tag{20}$$

$$\left(\vec{\boldsymbol{M}}_{A,ho}^{R}\right)_B = \sum_i \left(\vec{\boldsymbol{M}}_{A,ho}^{R_{FP_i}}\right)_B. \tag{21}$$

A blending factor κ is used to interpolate between the hover and wingborne aerodynamic models. The factor increases with airspeed and reaches $\kappa = 1$ in wingborne flight. The blended aerodynamic force and moment contributions are

$$\left(\vec{\boldsymbol{F}}_{A}^{R}\right)_B = (1-\kappa)\left(\vec{\boldsymbol{F}}_{A,ho}^{R}\right)_B + \kappa\left(\vec{\boldsymbol{F}}_{A,wb}^{R}\right)_B, \tag{22}$$

$$\left(\vec{\boldsymbol{M}}_{A}^{R}\right)_B = (1-\kappa)\left(\vec{\boldsymbol{M}}_{A,ho}^{R}\right)_B + \kappa\left(\vec{\boldsymbol{M}}_{A,wb}^{R}\right)_B. \tag{23}$$

The propulsion forces depend on the generated thrust and the corresponding tilt angles. For each propulsion unit, the thrust direction is rotated by the tilt mechanism, resulting in horizontal and vertical thrust components. The propulsive force contribution is expressed as

$$\left(\vec{\boldsymbol{F}}_{P}^{P_i}\right)_B = \begin{bmatrix} T_i\cos(\delta_i) \\ 0 \\ -T_i\sin(\delta_i) \end{bmatrix}_B, \tag{24}$$

and the total propulsive moment contribution is

$$\left(\vec{\boldsymbol{M}}_{P}^{R}\right)_B = \sum_i \left(\mathbf{M}_{BPf_i}\left(\vec{\boldsymbol{M}}_{P}^{P_i}\right)_{Pf_i} + \left(\vec{\boldsymbol{r}}^{RPf_i}\right)_B \times \left(\vec{\boldsymbol{F}}_{P}^{P_i}\right)_B\right), \tag{25}$$

where Pf_i is the i-th propulsion in the propulsion frame (Pf). The thrust of each propulsion unit is approximated by

$$T_i = \left(\frac{\omega_i}{2\pi}\right)^2 \rho d_i^4 c_{T_i}, \tag{26}$$

where ω_i is the rotational speed, d_i the propeller or impeller diameter, and c_{T_i} the thrust coefficient [19]. The corresponding torque is modeled as

$$\left(\vec{\boldsymbol{M}}_{P}^{P_i}\right)_{Pf_i} = \begin{bmatrix} 0 \\ 0 \\ \mathrm{sgn}(\omega_i)\left(\frac{\omega_i}{2\pi}\right)^2 \rho d_i^5 c_{Q_i} \end{bmatrix}_{Pf_i}, \tag{27}$$

with the torque coefficient c_{Q_i}. Finally, the gravitational force contribution is

$$\left(\vec{\boldsymbol{F}}_{G}^{R}\right)_B = \begin{bmatrix} -\sin\Theta \\ \sin\Phi\cos\Theta \\ \cos\Phi\cos\Theta \end{bmatrix} mg. \tag{28}$$

The aircraft reference point is chosen at the center of gravity, such that no additional gravitational moment contribution occurs.

2.4 Trimming and Linearization

The gain optimization procedure requires linear models at selected operating points. These operating points are obtained by trimming the nonlinear aircraft model. A trim point represents a steady flight condition in which the relevant state derivatives vanish and the total forces and moments are balanced.

In this work, trimming and linearization are performed using the trim-linearization-maneuverability-performance-controllability (TLMPC) toolbox [20, 21]. The toolbox provides a flexible interface for algebraic and state-space Simulink models and supports the formulation of trim problems through model definitions and trim templates. The model definition specifies the inputs, outputs, states, and parameters of the Simulink model, while the trim template defines the solver variables, equality constraints, bounds, and objectives.

The nonlinear equations of motion are represented in general state-space form as

$$\begin{cases} \dot{\mathbf{x}}(t) = \mathbf{f}(\mathbf{x}(t), \mathbf{u}(t)), \\ \mathbf{y}(t) = \mathbf{h}(\mathbf{x}(t), \mathbf{u}(t)). \end{cases} \tag{29}$$

The state vector contains translational velocities, angular rates, attitude angles, and position states (see Tab. 1).

Table 1 – State vector of the aircraft.

Velocity	Angular velocity		Attitude	Position
$\left(u_K^R\right)_B^E$	$\left(\omega_{K,x}^{OB}\right)_B$	p	Φ	x_0
$\left(v_K^R\right)_B^E$	$\left(\omega_{K,y}^{OB}\right)_B$	q	Θ	y_0
$\left(w_K^R\right)_B^E$	$\left(\omega_{K,z}^{OB}\right)_B$	r	Ψ	z_0

The input vector contains the commanded actuator variables of the propulsion units, tilt mechanisms, and aerodynamic surfaces. For each operating point, the trim solver determines a state-input combination $(\mathbf{x}_0, \mathbf{u}_0)$ that satisfies the steady-state condition

$$\dot{\mathbf{x}}_0 = \mathbf{f}(\mathbf{x}_0, \mathbf{u}_0) = \mathbf{0}. \tag{30}$$

Additional trim constraints are imposed depending on the considered flight condition. Typical constraints prescribe the desired airspeed, altitude, attitude angles, angular rates, and sideslip angle. Other quantities, such as the angle of attack or actuator positions, may be constrained by bounds rather than fixed to prescribed values. The overall trim conditions are represented in Tab. 2.

Table 2 – Trim objectives for the TLMPC toolbox.

States	Steady State	Known	States	Steady State	Known	Inputs	Known
p	✓	✓	u_K	✓	✘	$\mathbf{u}$[1]	✘
q	✓	✓	v_K	✓	✘		
r	✓	✓	w_K	✓	✘	Outputs	
Φ	✓	✘	x_0	✘	✓	α[1]	✘
Θ	✓	✘	y_0	✓	✓	β	✓
Ψ	✓	✓	z_0	✓	✓	V_A	✓

[1] The condition is unknown, but limitations are assigned

Around each trim point, the nonlinear dynamics are approximated by a first-order Taylor expansion. The resulting perturbation model is

$$\delta\dot{\mathbf{x}}(t) \approx \left.\frac{\partial \mathbf{f}}{\partial \mathbf{x}}\right|_{\mathbf{x}_0,\mathbf{u}_0} \delta\mathbf{x}(t) + \left.\frac{\partial \mathbf{f}}{\partial \mathbf{u}}\right|_{\mathbf{x}_0,\mathbf{u}_0} \delta\mathbf{u}(t), \tag{31}$$

with the output perturbation

$$\delta\mathbf{y}(t) \approx \left.\frac{\partial \mathbf{h}}{\partial \mathbf{x}}\right|_{\mathbf{x}_0,\mathbf{u}_0} \delta\mathbf{x}(t) + \left.\frac{\partial \mathbf{h}}{\partial \mathbf{u}}\right|_{\mathbf{x}_0,\mathbf{u}_0} \delta\mathbf{u}(t). \tag{32}$$

This yields the linear state-space representation

$$\begin{cases} \delta\dot{\mathbf{x}}(t) = \mathbf{A}\delta\mathbf{x}(t) + \mathbf{B}\delta\mathbf{u}(t), \\ \delta\mathbf{y}(t) = \mathbf{C}\delta\mathbf{x}(t) + \mathbf{D}\delta\mathbf{u}(t). \end{cases} \tag{33}$$

The matrices $\mathbf{A}$, $\mathbf{B}$, $\mathbf{C}$, and $\mathbf{D}$ are therefore obtained from the Jacobians of the nonlinear model at the selected trim point. From the full linearized model, the relevant input, output, and state channels are selected for the subsequent control design and gain optimization. In the present work, this linear model serves as the basis for the set of requirements introduced in the following sections.

3 Flight Control System

This section introduces the flight control system (FCS) architecture used for the gain-optimization framework. The controller follows a sensor-based INDI formulation and is implemented as a cascaded structure consisting of an outer-loop (OL) for translational velocity control and an inner-loop (IL) for attitude and angular-rate control. The corresponding core structure is shown in Fig. 2.

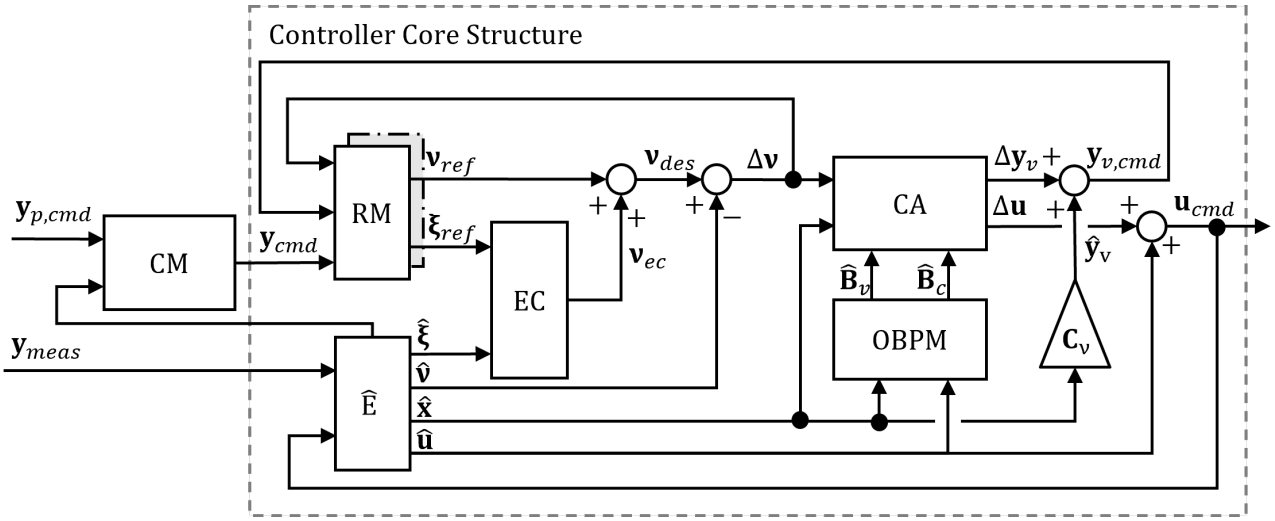


Figure 2 – Core structure of the cascaded sensor-based INDI controller.

The INDI core structure contains:

- Command mapping (CM): Maps the pilot commands to the command variables used by the inner and outer-loop control laws, ensuring a consistent command interface for the cascaded control architecture.
- Reference model (RM): Generates smooth reference trajectories for the inner and outer-loop and defines the desired command dynamics.
- Estimator (EST): Provides the estimated signals required by the controller, including filtered sensor data, state estimates, derivative estimates, and reconstructed actuator states when direct measurements are unavailable.

- Error controller (EC): Computes the pseudocontrol correction from the deviation between reference and estimated states, representing the main tuning element of the cascaded INDI controller.
- Control allocation (CA): Allocates the demanded pseudocontrol increments to the available effectors and converts them into actuator command increments.
- On-board plant model (OBPM): Provides the onboard plant model used to compute the local control effectiveness matrix of the effectors concerning the selected pseudocontrols.

3.1 Sensor-Based INDI Formulation

The INDI control law is derived from the local linear approximation of the nonlinear aircraft model around a trim point. Considering the nonlinear state-space model introduced in Eq. (29), a first-order Taylor approximation around the trim solution $(\mathbf{x}_0, \mathbf{u}_0)$ gives

$$\dot{\mathbf{x}} \approx \mathbf{f}(\mathbf{x}_0, \mathbf{u}_0) + \left.\frac{\partial \mathbf{f}}{\partial \mathbf{x}}\right|_{\mathbf{x}_0,\mathbf{u}_0} \Delta\mathbf{x} + \left.\frac{\partial \mathbf{f}}{\partial \mathbf{u}}\right|_{\mathbf{x}_0,\mathbf{u}_0} \Delta\mathbf{u} + h.o.t., \tag{34}$$

with

$$\Delta\mathbf{x} = \mathbf{x} - \mathbf{x}_0, \qquad \Delta\mathbf{u} = \mathbf{u} - \mathbf{u}_0. \tag{35}$$

At the trim point, the steady-state condition

$$\mathbf{f}(\mathbf{x}_0, \mathbf{u}_0) = \mathbf{0} \tag{36}$$

is fulfilled. Neglecting higher-order terms, the incremental state dynamics are therefore expressed as

$$\Delta\dot{\mathbf{x}} \approx \mathbf{A}\Delta\mathbf{x} + \mathbf{B}\Delta\mathbf{u}, \tag{37}$$

where

$$\mathbf{A} = \left.\frac{\partial \mathbf{f}}{\partial \mathbf{x}}\right|_{\mathbf{x}_0,\mathbf{u}_0}, \qquad \mathbf{B} = \left.\frac{\partial \mathbf{f}}{\partial \mathbf{u}}\right|_{\mathbf{x}_0,\mathbf{u}_0}. \tag{38}$$

For the controlled output vector $\mathbf{y}$, the corresponding incremental output derivative can be expressed in a compact form as

$$\Delta\dot{\mathbf{y}} \approx \mathbf{A}\Delta\mathbf{x} + \mathbf{B}\Delta\mathbf{u}. \tag{39}$$

Following the INDI formulation introduced in [22, 23], Eq. (39) is rewritten in terms of the pseudocontrol increment as

$$\Delta\boldsymbol{\nu} \approx \mathbf{A}_\nu\Delta\mathbf{x} + \mathbf{B}_\nu\Delta\mathbf{u}. \tag{40}$$

Here, $\mathbf{B}_\nu$ denotes the local control effectiveness matrix from actuator increments to pseudocontrol increments $\Delta\boldsymbol{\nu}$. In sensor-based INDI, the term $\mathbf{A}_\nu\Delta\mathbf{x}$ is not modeled explicitly. Instead, the current output derivative is obtained from measurements or estimates, while the model is only used to describe the incremental input contribution. This leads to

$$\Delta\boldsymbol{\nu} = \boldsymbol{\nu}_{des} - \hat{\boldsymbol{\nu}} \approx \hat{\mathbf{B}}_\nu\Delta\mathbf{u}. \tag{41}$$

Using the time-scale separation assumption, the incremental control input can be designed while neglecting the state-dependent term [24, 25]. This approximation is justified for sufficiently high control update rates, for which the state deviation remains small and $\mathbf{x}$ stays close to $\mathbf{x}_0$ over one control update [23]. Measured or estimated quantities in Eq. (41) are therefore denoted by the hat operator ('^'). The desired actuator increment is then obtained by solving the control allocation problem

$$\Delta\mathbf{u} = \hat{\mathbf{B}}_\nu^{+}\Delta\boldsymbol{\nu}, \tag{42}$$

where $\hat{\mathbf{B}}_v^+$ denotes the Moore–Penrose pseudoinverse. The use of a pseudoinverse allows the formulation to handle overactuated or underactuated configurations. If $\mathbf{B}_v$ is square and nonsingular, the pseudoinverse reduces to the ordinary inverse. The commanded actuator vector is finally obtained from

$$\mathbf{u}_{cmd} = \hat{\mathbf{u}} + \Delta\mathbf{u}. \tag{43}$$

The current control input $\hat{\mathbf{u}}$ is either measured directly, provided that the corresponding effector supports such measurements, or reconstructed using an effector model. If all control inputs are available from measurements, the formulation is referred to as strict sensor-based INDI [9]. This incremental formulation reduces the dependency on a complete model of the aircraft dynamics. The dominant model dependency is shifted to the local control effectiveness matrix $\mathbf{B}_v$, while unmodeled state-dependent terms are compensated through the measured or estimated output derivatives.

3.2 Cascaded INDI Architecture

The *PEGASUS* controller uses a cascaded INDI architecture. The outer-loop controls the translational motion, whereas the inner-loop controls attitude and angular rates. The pilot command vector is defined as

$$\mathbf{y}_{p,cmd} = \begin{bmatrix} \left(\vec{V}_K^G\right)_C^E \\ \dot{\Psi} \end{bmatrix}_{cmd}. \tag{44}$$

The translational velocity commands are expressed in the control frame C, which is obtained by rotating the local navigation frame about the yaw angle Ψ [26]. The commanded heading-rate contribution Ψ_{cmd} is passed to the inner-loop, where it is used either to initiate coordinated turning behavior in wingborne flight or to command yaw motion in hover.

The pilot commands are shaped by reference models before entering the ECs. The outer-loop RM has a relative degree of one and generates desired translational acceleration-related pseudocontrols. The inner-loop RM has a relative degree of two for roll and pitch attitude commands and a relative degree of one for yaw-rate commands. The resulting reference pseudocontrol vector is

$$\boldsymbol{\nu}_{ref} = \begin{bmatrix} \vec{n}_C \\ \left(\dot{\vec{\omega}}_K^{OB}\right)_B^B \end{bmatrix}_{ref}, \tag{45}$$

where $\vec{n}_C$ denotes the commanded load-factor vector in the control frame and $\left(\dot{\vec{\omega}}_K^{OB}\right)_B^B$ denotes the commanded body angular acceleration vector.

The outer-loop generates virtual control inputs for the inner-loop. In the present architecture, these virtual control inputs are the roll and pitch attitude commands,

$$\mathbf{y}_{\nu,cmd} = \begin{bmatrix} \Phi \\ \Theta \end{bmatrix}_{\nu,cmd}. \tag{46}$$

This structure allows the same high-level command interface to be used across hover, transition, and wingborne flight, while the control allocation and the controller gains adapt the actuator usage to the current operating conditions.

The RM parameters used in the baseline controller are summarized in Tab. 3. These parameters define the desired command dynamics and are kept fixed during the gain optimization considered in this work.

The RM characteristics are kept fixed throughout the considered flight envelope and represent a compromise between hover and wingborne operations. Both the inner-loop and outer-loop parameters are selected to provide sufficiently responsive command dynamics while limiting actuator activity. Although the propulsors are primarily oriented in the vertical direction during hover, the vertical-velocity time constant T_w is chosen to be equal to the lateral-velocity time constant T_v. This avoids unnecessarily aggressive vertical command dynamics, which would otherwise require fast thrust variations and increased propulsion usage.

Table 3 – Reference model parametrization.

Outer-loop time constants for $[u\ v\ w]_C$		
$T_u = 1.5$ s	$T_v = 2.0$ s	$T_w = 2.0$ s
Inner-loop natural frequencies and time constant for $[p\ q\ r]_B$		
$\omega_{0,p} = 5$ rad/s	$\omega_{0,q} = 5$ rad/s	$T_r = 0.75$ s
Inner-loop damping ratios for $[p\ q\ r]_B$		
$\zeta_p = 0.8$	$\zeta_q = 0.8$	–

3.3 Error Controller

The EC is the main tuning element in the considered FCS. It compares the reference state $\boldsymbol{\xi}_{ref}$ from the RM with the estimated state $\hat{\boldsymbol{\xi}}$ and generates an additional pseudocontrol contribution. In this work, the EC is implemented as a proportional controller,

$$\boldsymbol{\nu}_{ec} = \mathbf{K}_P \left(\boldsymbol{\xi}_{ref} - \hat{\boldsymbol{\xi}} \right), \tag{47}$$

where $\mathbf{K}_P$ is a diagonal gain matrix. The proportional structure is sufficient for the considered INDI formulation because the control law is based on increments and uses measured or estimated state derivatives. Consequently, the EC primarily shapes the desired closed-loop error dynamics, while the incremental update compensates for part of the model mismatch and disturbance effects.

The cascaded architecture contains one EC in the outer loop and one in the inner loop. The outer-loop EC generates translational pseudocontrol corrections from velocity tracking errors. Its gains are collected in

$$\mathbf{K}_{P,vel} = \mathrm{diag}\left(k_{p,u}, k_{p,v}, k_{p,w}\right). \tag{48}$$

The outer-loop gains determine the response of the translational motion and provide attitude-related commands to the inner loop in the allocation. To support time-scale separation, the outer-loop dynamics are chosen to be slower than the inner-loop dynamics.

The inner-loop EC generates pseudocontrol corrections for attitude and angular rate. Its gains are separated into contributions for attitude and rate,

$$\mathbf{K}_{P,att} = \mathrm{diag}\left(k_{p,\Phi}, k_{p,\Theta}, 0\right), \qquad \mathbf{K}_{P,rot} = \mathrm{diag}\left(k_{p,p}, k_{p,q}, k_{p,r}\right). \tag{49}$$

The attitude gains shape the response to roll and pitch attitude errors, while the rate gains shape the angular-rate dynamics. The inner-loop is designed to be faster than the outer-loop so that the vehicle can accurately follow the virtual commands generated by the translational controller.

The control effectiveness and aircraft dynamics vary significantly over the flight envelope, especially during transition. Aerodynamic surfaces become increasingly effective with airspeed, while the relative contribution of propulsion-based control decreases. Therefore, a single fixed gain set is not sufficient to provide consistent performance in hover, transition, and wingborne flight.

4 Optimization Workflow

This section describes the proposed workflow for tuning the cascaded INDI controller introduced in Section 3. The objective of the workflow is to determine suitable controller gains for selected operating points such that the resulting closed-loop system satisfies prescribed performance and robustness requirements. The overall process is summarized in Fig. 3.

The workflow consists of three main steps. First, the user defines the design case and the associated requirements. A design case specifies the operating condition at which the controller shall be tuned, for example by prescribing altitude and airspeed. Based on the selected operating point, the

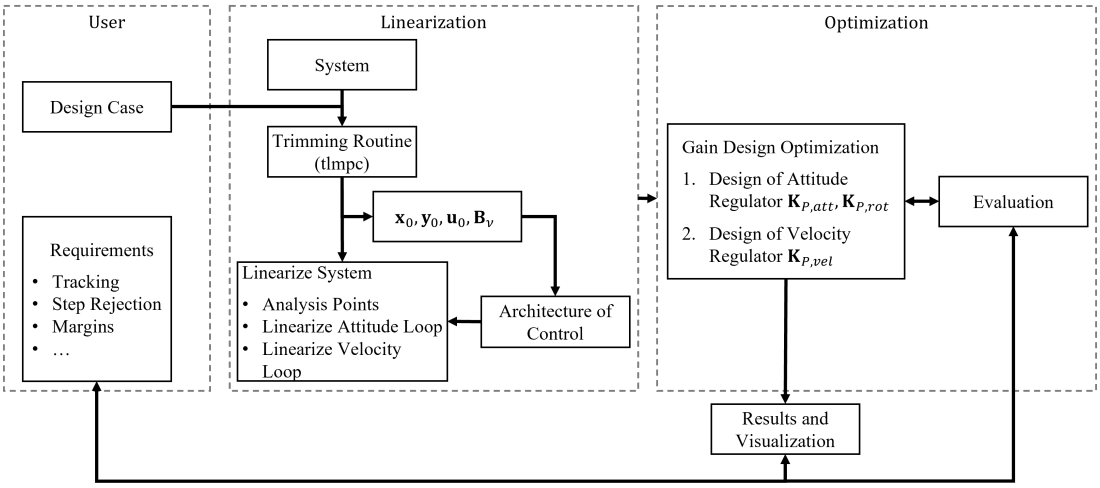


Figure 3 – Gain-design optimization workflow for the cascaded INDI controller.

corresponding flight phase, i.e. hover, transition, or wingborne flight, can be identified. If multiple operating points are considered, the same procedure is repeated for each point. The requirements are formulated as frequency-domain or time-domain performance and robustness conditions, together with optional structural constraints on the gain vector.
Second, the nonlinear aircraft model is trimmed and linearized at the specified design condition. As described in Section 2.4, the TLMPC toolchain is used to compute a trim point and to obtain a local linear state-space representation. The resulting linear model provides the aircraft dynamics, the trimmed states and inputs, and the local control effectiveness matrix $\mathbf{B}_v$. Since the FCS is cascaded, separate linear closed-loop interconnections are constructed for the inner and outer-loops. These linear environments are used to evaluate the tuning requirements during the optimization.
Third, the gain optimization is performed iteratively. The inner-loop gains are tuned first because the outer-loop dynamics rely on the response of the inner-loop. After the inner-loop gains have been determined, they are fixed and the outer-loop gains are optimized. During each iteration, the optimizer updates the gain vector and evaluates the requirements on the corresponding linear system. The best feasible solution is retained and used as the tuned gain set for the considered operating point.

4.1 Linear Optimization Environment

The optimization is performed on a linear closed-loop representation of the aircraft and controller. The structure of the linear environment is shown in Fig. 4. It contains the linearized aircraft model, actuator dynamics, transport delays, estimator dynamics, and the linearized INDI controller. The same environment is used to define analysis points for evaluating tracking, disturbance rejection, and robustness requirements.
The actuator dynamics map the commanded actuator vector $\mathbf{u}_{cmd}$ to the actual actuator vector $\mathbf{u}$ according to

$$\mathbf{u}(s) = \mathbf{G}_{uu_{cmd}}(s)\mathbf{u}_{cmd}(s). \tag{50}$$

Depending on the actuator type, $\mathbf{G}_{uu_{cmd}}(s)$ is represented by first- or second-order transfer functions. Propulsion dynamics are modeled as first-order systems, whereas tilt mechanisms and aerodynamic control surfaces are represented by second-order systems [17, 16]. Additional actuator limits are not directly part of the linear transfer function, but may be considered through gain constraints or subsequent nonlinear validation.
Disturbances are included through the wind input. The wind vector enters the aircraft model through the aerodynamic velocity relation and is represented in the linear environment by

$$\mathbf{y}_d(s) = \mathbf{G}_{y_d V_W}(s)\vec{\boldsymbol{V}}_W(s) = \mathbf{G}_{y_d d}(s)\vec{\boldsymbol{d}}(s), \tag{51}$$

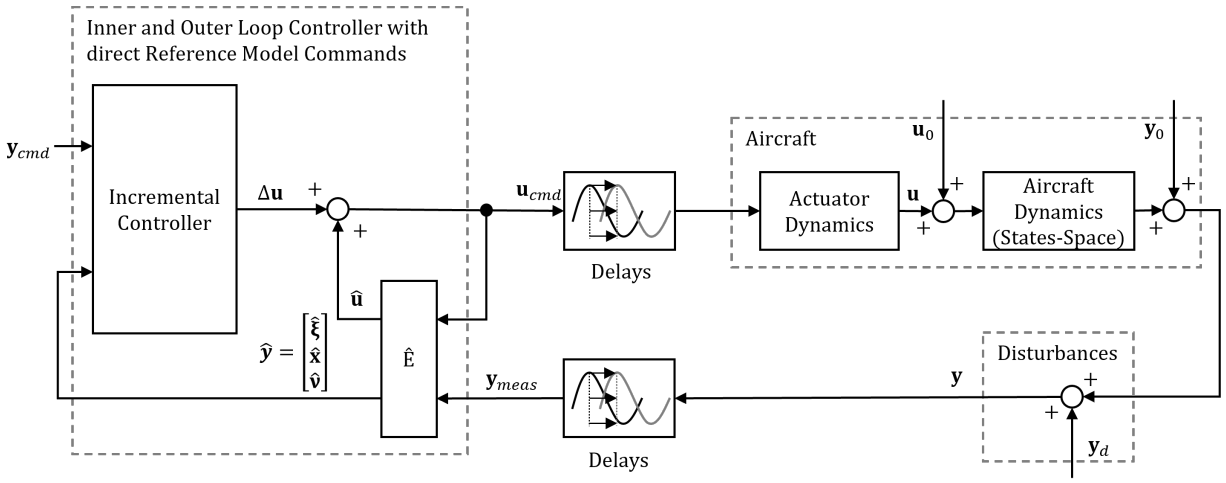


Figure 4 – Linear closed-loop environment including actuator dynamics, aircraft dynamics, transport delays, estimator dynamics, disturbances, and the cascaded INDI controller.

where $\vec{\boldsymbol{d}}(s)$ denotes the disturbance input vector. The linearized aircraft dynamics are therefore written as

$$\mathbf{y}(s) = \mathbf{G}_{yu}(s)\mathbf{u}(s) + \mathbf{G}_{y_d d}(s)\vec{\boldsymbol{d}}(s). \tag{52}$$

Transport delays are included to approximate the behavior of the embedded implementation. These delays account for signal transmission, sampling, and computation effects. A delay with time constant T_s is represented by

$$\mathbf{G}_{delay}(s) = e^{-sT_s}. \tag{53}$$

Since Eq. (53) describes an infinite-dimensional system, the delay is approximated by a rational transfer function for linear analysis. In this work, a Padé approximation is used [27].
The estimator maps measured signals to estimated variables required by the controller. Its linear representation is written as

$$\hat{\mathbf{y}}(s) = \mathbf{G}_{\hat{y}y_{meas}}(s)\mathbf{y}_{meas}(s). \tag{54}$$

The estimator transfer function includes the relevant sensor filters, complementary filters, and actuator estimation dynamics [28, 29]. These dynamics are important for the tuning process because they influence the frequency response between command, feedback, and pseudocontrol signals.
The command vector of the cascaded control system is separated into inner- and outer-loop commands,

$$\mathbf{y}_{cmd} = \begin{bmatrix} \mathbf{y}_{IL,cmd} \\ \mathbf{y}_{OL,cmd} \end{bmatrix}, \tag{55}$$

with

$$\mathbf{y}_{IL,cmd} = \begin{bmatrix} \Phi \\ \Theta \\ \dot{\Psi} \end{bmatrix}_{cmd}, \qquad \mathbf{y}_{OL,cmd} = \begin{bmatrix} u_C \\ v_C \\ w_C \end{bmatrix}_{cmd}. \tag{56}$$

The inner-loop command vector contains roll attitude, pitch attitude, and heading-rate commands. The outer-loop command vector contains translational velocity commands in the control frame. Depending on the tuning step, either the inner-loop or outer-loop command channels are selected as analysis inputs for the corresponding requirement evaluation.

4.2 Optimization Problem

The gain tuning task is formulated as a constrained optimization problem. The tunable parameters are collected in the vector $\mathbf{p}$, which contains the selected entries of the error-controller gain matrices introduced in Section 3.3. For each operating point, the optimizer searches for a gain vector that minimizes the weighted sum of soft objectives while satisfying all hard constraints and bounds.
The optimization problem is formulated as

$$\begin{aligned} \min_{\mathbf{p}} \quad & \sum_{i=1}^{N_f} w_i f_i(\mathbf{p}) \\ \text{s.t.} \quad & g_j(\mathbf{p}) \leq 1, \qquad j = 1,\ldots,N_g, \\ & \mathbf{A}_{ineq}\mathbf{p} - \mathbf{b}_{ineq} \leq \mathbf{0}, \\ & \underline{\mathbf{p}} \leq \mathbf{p} \leq \overline{\mathbf{p}}. \end{aligned} \tag{57}$$

The functions $f_i(\mathbf{p})$ denote soft objectives, which are minimized according to their weighting factors w_i. The functions $g_j(\mathbf{p})$ denote hard requirements. A gain vector is considered feasible only if all hard requirements satisfy $g_j(\mathbf{p}) \leq 1$. This normalization allows different requirements, such as tracking performance and robustness margins, to be evaluated within a common framework.
The lower and upper bounds $\underline{\mathbf{p}}$ and $\overline{\mathbf{p}}$ restrict the admissible gain range. In addition, the matrix $\mathbf{A}_{ineq}$ and vector $\mathbf{b}_{ineq}$ impose linear inequality constraints on the gain vector. These constraints can be used to enforce structural relations between gains. For example, the angular-rate dynamics in the inner-loop are required to be faster than the attitude dynamics. This can be reflected by imposing suitable inequalities between the corresponding attitude and rate gains.
Each requirement is represented by a scalar cost function,

$$\begin{aligned} f_i(\mathbf{p}) &:= J_i(\mathbf{p}), \qquad i \in \mathcal{I}, \\ g_j(\mathbf{p}) &:= J_j(\mathbf{p}), \qquad j \in \mathcal{J}. \end{aligned} \tag{58}$$

This formulation makes it possible to treat tracking, disturbance rejection, robustness, and structural requirements consistently. Requirements that must be fulfilled are assigned to the hard-constraint set $\mathcal{J}$, whereas requirements that should be improved as far as possible are assigned to the soft-objective set $\mathcal{I}$.

4.3 Particle Swarm Optimization

The optimization problem in Eq. (57) is solved using PSO [30, 31]. This population-based metaheuristic is well suited for the present gain-tuning problem because it does not require gradient information and can handle non-smooth objective functions arising from frequency-domain norm evaluations and constraint penalties.
Each particle represents one candidate gain vector $\mathbf{p}_k \in \mathbb{R}^{n_p}$ at iteration k. The particle also has a velocity vector $\mathbf{v}_k \in \mathbb{R}^{n_p}$ that determines its movement through the search space. The velocity and position are updated according to

$$\begin{aligned} \mathbf{v}_{k+1} &= \mathbf{I}\mathbf{v}_k + c_1\mathbf{r}_1 \odot \left(\mathbf{p}^{\star}_{self} - \mathbf{p}_k\right) + c_2\mathbf{r}_2 \odot \left(\mathbf{p}^{\star}_{neighbour} - \mathbf{p}_k\right) \\ \mathbf{p}_{k+1} &= \mathbf{p}_k + \mathbf{v}_{k+1}. \end{aligned} \tag{59}$$

Here, $\mathbf{I}$ denotes the inertia or constriction factor, while c_1 and c_2 are the acceleration coefficients. The random vectors $\mathbf{r}_1$ and $\mathbf{r}_2$ are resampled at each iteration, typically with uniformly distributed entries in the interval $[0,1]$. The vector $\mathbf{p}^{\star}_{self}$ is the best position previously found by the particle itself, whereas $\mathbf{p}^{\star}_{neighbour}$ is the best position found within the selected neighborhood topology.
The first attraction term in Eq. (59) represents the cognitive component, which pulls the particle toward its own best solution. The second attraction term represents the social component, which pulls the particle toward the best solution communicated by the swarm or its neighborhood. Hence, the particles are not moved directly to the current best solution, but are gradually accelerated toward promising regions while retaining part of their previous motion.

Constraints are handled by a penalty strategy. For each particle, all hard requirements and linear inequality constraints are evaluated after the gain vector has been applied to the linear closed-loop model. If a particle satisfies all constraints, its objective value is computed from the weighted soft-objective sum in Eq. (57). If one or more constraints are violated, the objective value is augmented by a penalty term.
The penalty formulation biases the swarm toward feasible regions while still allowing for temporary exploration close to constraint boundaries. After convergence, the selected gain vector is the feasible solution with the lowest penalized cost. If no feasible particle is found, the solution with the smallest total constraint violation is retained for further inspection [32].

5 Requirements

This section defines the requirements used in the gain-optimization framework. The requirements are configured by the user for each design case introduced in Section 4. They are evaluated in the linear closed-loop environment described in Section 4.1 and are converted into scalar cost functions for the optimization problem in Eq. (57).
The requirements are divided into two groups. Closed-loop requirements are used to shape command tracking, disturbance rejection, and practical achievability. Open-loop requirements are used to enforce robustness margins at selected loop-breaking points. Before performance requirements are evaluated, closed-loop stability is checked by verifying that all poles of the linear closed-loop system lie in the stable region. If this condition is violated, the corresponding gain vector is treated as infeasible.

5.1 Closed-Loop Requirements

Following the standard notation in [29, 33], with a nominal plant $G(s)$ and controller $K(s)$, the open-loop transfer function is

$$L(s) = G(s)K(s). \tag{60}$$

The sensitivity and complementary sensitivity functions are defined as

$$\begin{aligned} S(s) &= (I + L(s))^{-1}, \\ T(s) &= L(s)\,(I + L(s))^{-1}. \end{aligned} \tag{61}$$

Although the notation is introduced for a single-input single-output (SISO) channel, the same definitions are applied to selected input-output channels of the mulitple-input multiple-output (MIMO) closed-loop system. The output response with disturbance input $d(s)$ is transferred via the disturbance transfer function $G_d(s)$ and the plant input $u(s)$:

$$y(s) = G(s)u(s) + G_d(s)d(s). \tag{62}$$

For a reference command $r(s)$, Eq. (62) can be rewritten as

$$y(s) = T(s)r(s) + S(s)G_d(s)d(s), \tag{63}$$

using the formalism in Eq. (61) [27]. The control error is given by

$$e(s) = y(s) - r(s) = -S(s)r(s) + S(s)G_d(s)d(s) \tag{64}$$

The scalar requirement functions are primarily based on $\mathcal{H}_\infty$-norms. For a stable transfer function, the $\mathcal{H}_\infty$-norm corresponds to the worst-case amplification over all frequencies [34, 29],

$$\begin{cases} ||S(s)||_\infty \triangleq \max\limits_{\omega} |S(j\omega)| &= \overline{\sigma}_S, \\ ||T(s)||_\infty \triangleq \max\limits_{\omega} |T(j\omega)| &= \overline{\sigma}_T, \end{cases} \tag{65}$$

with the maximum singular value over all frequencies $\overline{\sigma}$. In the MIMO case, the peak is evaluated with respect to the largest singular value. This makes the $\mathcal{H}_\infty$-norm suitable for robust performance requirements, since it limits the largest possible amplification in the considered frequency range. The $\mathcal{H}_2$-norm is additionally used for selected transient-shaping objectives. For a stable and strictly proper transfer function, it is defined as

$$\|T(s)\|_2 \triangleq \left(\frac{1}{2\pi}\int_{-\infty}^{\infty}|T(j\omega)|^2 d\omega\right)^{1/2} = h_{2,T}. \tag{66}$$

While the $\mathcal{H}_\infty$-norm constrains the worst-case response, the $\mathcal{H}_2$-norm measures the overall input-output energy and is therefore useful for average amplification and transient-response objectives [35].

5.1.1 Tracking

Tracking requirements compare the achieved closed-loop response with the desired reference behavior. In the cascaded INDI architecture, the reference behavior is defined by the corresponding RM. For a selected command-output channel, the tracking error transfer function is

$$e_T(s,\mathbf{p}) = T_{\hat{y}y_{cmd}}(s,\mathbf{p}) - T_{ref}(s), \tag{67}$$

where $T_{\hat{y}y_{cmd}}(s,\mathbf{p})$ is the closed-loop transfer function obtained with the gain vector $\mathbf{p}$, and $T_{ref}(s)$ denotes the desired reference-model dynamics. The admissible tracking error is specified by a frequency-dependent error profile,

$$W_{e,T}(s) = \frac{\overline{e}_T s + \omega_{ce}\underline{e}_T}{s+\omega_{ce}}. \tag{68}$$

Here, $\underline{e}_T$ defines the admissible low-frequency tracking error, $\overline{e}_T$ defines the admissible high-frequency tracking error, and ω_{ce} defines the crossover frequency [36, 37]. The shape of Eq. (68) is visualized by Fig. 5.

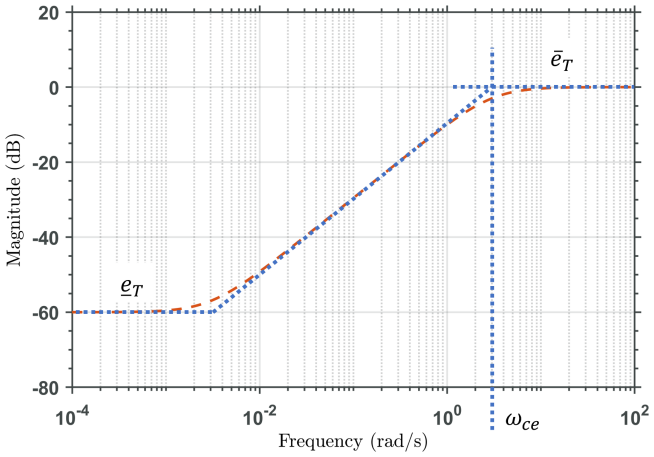


Figure 5 – Tracking-error weighting over frequency with $\overline{e}_T = 1$, $\underline{e}_T = 10^{-4}$, and $\omega_{ce} = 3$ rad/s.

Small low-frequency values enforce accurate tracking in the command bandwidth, whereas larger high-frequency values avoid unnecessary tracking of high-frequency content, such as sensor noise or unmodeled dynamics. The corresponding tracking cost is formulated as

$$J_k(\mathbf{p}) = \left\| \frac{1}{W_{e,T}(s)} \left(T_{\hat{y}y_{cmd}}(s,\mathbf{p}) - T_{ref}(s)\right) \right\|_\infty. \tag{69}$$

The tracking requirement is satisfied if

$$J_k(\mathbf{p}) \leq 1. \tag{70}$$

For channels with zero steady-state gain, a direct DC-normalized tracking requirement may not be meaningful. In such cases, an alternative step-response matching criterion is used. The corresponding $\mathcal{H}_2$-based cost is

$$J_k(\mathbf{p}) = \frac{\left\| \hat{y}(t,\mathbf{p}) - y_{ref}(t) \right\|_2}{\varepsilon_{rel} \left\| y_{ref}(t) \right\|_2}, \tag{71}$$

, with the relative gap ε_{rel}. This criterion compares the achieved and desired step responses in terms of their response energy and can therefore be used for transient-shaping objectives [35].

5.1.2 Disturbance Rejection

Disturbance-rejection requirements constrain the closed-loop response from the disturbance input to selected controlled outputs. In the present application, the disturbance input represents wind components introduced in the linear environment. The relevant transfer function from the disturbance input to the estimated controlled output is denoted by $T_{\hat{y}d}(s,\mathbf{p})$. For zero reference command, the disturbance-induced error is therefore given by

$$e_{DR}(s,\mathbf{p}) = T_{\hat{y}d}(s,\mathbf{p}). \tag{72}$$

The admissible disturbance-induced error is specified by the weighting function

$$W_{e,DR}(s) = \frac{\overline{e}_{DR} s + \omega_{ce} \underline{e}_{DR}}{s + \omega_{ce}}, \tag{73}$$

where $\underline{e}_{DR}$ defines the admissible low-frequency error, $\overline{e}_{DR}$ defines the admissible high-frequency error, and ω_{ce} determines the transition frequency between both bounds. For the disturbance step-rejection requirement, the transition frequency is selected based on the corresponding decay time constant as

$$\omega_{ce} = \frac{1}{\tau_{DR}}. \tag{74}$$

If the disturbance-rejection requirement is specified by a decay time T_{DR} and a relative tolerance band ε_{DR}, the corresponding first-order time constant is

$$\tau_{DR} = \frac{T_{DR}}{|\ln(\varepsilon_{DR})|}. \tag{75}$$

This formulation allows the disturbance-rejection objective to be specified from a time-domain interpretation while still being evaluated in the frequency domain. The disturbance-rejection cost is then

$$J_k(\mathbf{p}) = \left\| \frac{1}{W_{e,DR}(s)} T_{\hat{y}d}(s,\mathbf{p}) \right\|_\infty. \tag{76}$$

The requirement is fulfilled if

$$J_k(\mathbf{p}) \leq 1. \tag{77}$$

This condition ensures that the magnitude of the disturbance-induced response remains below the admissible error profile $W_{e,DR}(s)$ over the considered frequency range.

5.1.3 Practical Achievability

Practical achievability requirements are used to limit the amplification of selected internal signals. In the present framework, this requirement is mainly used to reduce excessive actuator usage caused by disturbances. The relevant transfer function from the disturbance input to the actuator increment commanded by the CA is denoted by $T_{\Delta ud}(s,\mathbf{p})$.

To account for actuator limitations, the actuator increments are normalized with respect to their admissible ranges. The weighting function is written as

$$W_S(s) = \frac{\overline{e}_S s + \omega_{ce}\underline{e}_S}{s + \omega_{ce}}. \tag{78}$$

The practical achievability cost is defined as

$$J_k(\mathbf{p}) = \left\| \frac{1}{W_S(s)} T_{\Delta ud}(s,\mathbf{p}) \right\|_\infty. \tag{79}$$

The corresponding requirement is satisfied for

$$J_k(\mathbf{p}) \leq 1. \tag{80}$$

This requirement prevents the optimizer from achieving good tracking or disturbance rejection at the cost of excessive actuator activity.

5.2 Open-Loop Requirements

Open-loop requirements are used to enforce robustness margins at selected loop-breaking points. In this work, disk margins are employed instead of classical gain and phase margins. Disk margins account for simultaneous gain and phase variations and therefore provide a more informative robustness measure for practical multivariable control systems [38].

The disk margin is characterized by the disk size α and the skew parameter σ. The disk size describes the admissible uncertainty radius, while the skew parameter determines whether the uncertainty is biased toward gain increase or gain decrease. In this work, the balanced case $\sigma = 0$ is used, corresponding to symmetric gain variations in a logarithmic sense.

For desired classical gain and phase margins, the corresponding balanced disk size can be approximated by

$$\alpha = 2\max\left\{ \frac{GM-1}{GM+1}, \tan\left(\frac{PM}{2}\right) \right\}. \tag{81}$$

Eq. (81) includes both gain and phase margins. The resulting value of α defines the required simultaneous gain-and-phase perturbation set for which robust closed-loop stability must be preserved [39, 38].

For the balanced case, the disk-margin robustness condition can be expressed through the sensitivity and complementary sensitivity functions as

$$\alpha_{\max} = \left\| \frac{1}{2}\left(S(j\omega,\mathbf{p}) - T(j\omega,\mathbf{p})\right) \right\|_\infty^{-1}. \tag{82}$$

This relation is useful for optimization because the desired disk-margin condition can be converted into an $\mathcal{H}_\infty$-type inequality. The corresponding disk-margin cost is formulated as

$$J_k(\mathbf{p}) = \left\| \frac{\alpha}{2}\left(S(j\omega,\mathbf{p}) - T(j\omega,\mathbf{p})\right) \right\|_\infty. \tag{83}$$

In the MIMO case, the corresponding equation is obtained as follows::

$$J_k(\mathbf{p}) = \left\| \alpha \mathbf{D}^{-1}\left(\mathbf{S}(j\omega,\mathbf{p}) - \frac{1}{2}\mathbf{I}\right)\mathbf{D} \right\|_\infty, \tag{84}$$

with scaling matrix $\mathbf{D}$ [38]. The robustness requirement is satisfied if

$$J_k(\mathbf{p}) \leq 1. \tag{85}$$

In the proposed tuning workflow, the loop is opened in front of the control allocation at the pseudocontrol increment $\Delta\boldsymbol{\nu}$. For the inner-loop, the corresponding loop-breaking points are shown in Fig. 6.

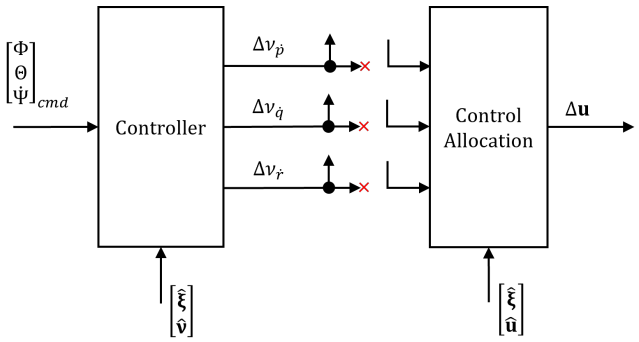


Figure 6 – Open-loop cuts for the inner-loop disk-margin evaluation in front of the control allocation.

5.3 Requirement Configuration

The tuning objectives used in the optimization are summarized in Tab. 4. Soft objectives f_i are minimized after feasibility has been established, whereas hard constraints g_j must satisfy the normalized bound $g_j(\mathbf{p}) \leq 1$. The hard constraints therefore primarily ensure stability and robustness, while the soft objectives improve tracking, disturbance rejection, and actuator usage.
The tracking weightings use the reference-model bandwidth as the characteristic transition frequency. The low-frequency error bound is selected to enforce accurate command following, while the high-frequency bound prevents the optimizer from unnecessarily tracking high-frequency dynamics. For disturbance rejection, the weighting parameters are derived from prescribed decay times and tolerable disturbance amplitudes. The wind disturbances used for tuning are summarized in Tab. 5.

Table 4 – Tuning goals used in the gain optimization.

Tuning goal	Type	Evaluation channel	Target
		Inner-loop	
Tracking of $\boldsymbol{\xi}_{ref}$[1]	f_1–f_5	$\hat{\boldsymbol{\xi}} - \boldsymbol{\xi}_{ref}$	Minimize[2]
Disturbance rejection	f_6–f_{11}	$\boldsymbol{\xi}_{err}$	Minimize[3]
Practical achievability	f_{12}	$\Delta\mathbf{u}$ from wind disturbance	Minimize
Inequality constraints	f_{13}	$\mathbf{K}_{P,att}$, $\mathbf{K}_{P,rot}$	$(K_{P,att})_{ii} < (K_{P,rot})_{ii}$
Disk margin	g_1	$\Delta\boldsymbol{\nu}_{IL}$	$GM > 3\,\mathrm{dB}$, $PM > 30^\circ$
		Outer-loop	
Tracking of $\boldsymbol{\xi}_{ref}$	f_{14}–f_{16}	$\hat{\boldsymbol{\xi}} - \boldsymbol{\xi}_{ref}$	Minimize[2]
Disturbance rejection	f_{17}–f_{19}	$\boldsymbol{\xi}_{err}$	Minimize[3]
Practical achievability	f_{20}	$\Delta\mathbf{u}$ from wind disturbance	Minimize
Disk margin	g_2	$\Delta\boldsymbol{\nu}_{OL}$	$GM > 3\,\mathrm{dB}$, $PM > 30^\circ$

[1] Yaw angle Ψ is not regulated.
[2] Error weighting characteristics: $\bar{e}_T = 2$, $\underline{e}_T = 10^{-3}$, ω_{ce} w.r.t. RM.
[3] Time constants: $T_{DR,att} = 3$ s, $T_{DR,rot} = 1.5$ s, $T_{DR,vel} = 3$ s.
Tolerable disturbance amplitudes: $\bar{e}_{DR,att} = 10^\circ$, $\bar{e}_{DR,rot} = 40^\circ/\mathrm{s}$, $\bar{e}_{DR,vel} = 2$ m/s.

Table 5 – Wind disturbance velocities used for controller optimization.

Symbol	Gust speed
u_W	$\pm 5\,\mathrm{m/s}$
v_W	$\pm 5\,\mathrm{m/s}$
w_W	$\pm 3\,\mathrm{m/s}$

5.4 Post-Optimization Linear Assessment

After the nominal gain optimization has converged, the resulting controller is further assessed using the linear closed-loop environment introduced in Section 4.1. This post-optimization assessment is not part of the optimization itself, but is used to analyze the behavior of the optimized gain set in greater detail. In this way, the optimization problem remains transparent and computationally efficient, while additional performance and robustness properties can still be investigated before nonlinear validation or flight testing.

The assessment is carried out in both the time and frequency domain. In the time domain, step responses are evaluated to inspect command tracking, transient behavior, settling characteristics, overshoot, and the influence of disturbances. These responses provide an intuitive interpretation of the optimized controller behavior and complement the frequency-domain requirements used during the optimization. In the frequency domain, closed-loop transfer functions, sensitivity functions, practical-achievability transfer functions, singular values, and open-loop robustness margins are analyzed. This allows the user to identify critical frequency ranges, coupling effects, and possible robustness limitations of the optimized controller.

In addition to the nominal model, perturbed linear models are considered to assess the sensitivity of the optimized gain set to modeling errors.

Aerodynamic uncertainties are especially relevant for aircraft operating in complex flight regimes, such as fixed-wing eVTOLs during transition, where the aircraft may operate close to stall speed and where aerodynamic and propulsive effects interact strongly. In this regime, deviations between the predicted model and the real aircraft behavior are expected. Previous studies, therefore, introduce variations of aerodynamic derivatives in order to account for model uncertainty. For example, variations of approximately $10\,\%$ for longitudinal derivatives and up to $30\,\%$ for lateral derivatives are considered in [40, 41]. Other studies apply uncertainty ranges of about 10–$20\,\%$ to aerodynamic derivatives in general [42, 43]. Furthermore, the comparison between computational fluid dynamics and wind-tunnel measurements in [44] indicates that several aerodynamic derivatives agree within approximately 5–$15\,\%$, while selected derivatives, such as $C_{m\alpha}$ near $\alpha \approx 0^\circ$, may deviate by about 30–$40\,\%$. Based on these observations, uncertainty levels of up to $30\,\%$ are considered for selected longitudinal and lateral aerodynamic derivatives in the post-optimization analysis.

Mass-property and propulsion uncertainties are considered as additional perturbation classes in the post-optimization analysis. Mass-property variations account for payload changes, manufacturing tolerances, center-of-gravity shifts, and deviations in the assumed mass distribution. In [42], uncertainty levels of $2\,\%$ are assigned to mass, inertia, and center-of-mass parameters. For an eVTOL in vertical flight, [45] investigates a $10\,\%$ multiplicative uncertainty in the inertia matrix, applied only to the plant model while the controller and allocation mapping remain nominal.

Propulsion-related uncertainties are introduced through variations in the thrust and torque coefficients C_T and C_Q. For electric UAV propellers, [46] reports thrust-prediction errors of up to $15.06\,\%$ when the propeller speed is not directly measured. For small UAV propeller simulations, [47] reports power-coefficient deviations of up to $10.75\,\%$, which are used as an indication for torque-coefficient uncertainty. Based on these findings, C_T and C_Q are varied by $\pm 15\,\%$ in the post-optimization linear assessment.

The uncertainties discussed previously are summarized in Tab. 6.

Table 6 – Worst-case uncertainty levels used for the post-optimization linear assessment.

Uncertainty class	Parameters	Worst-case variation
Aerodynamics	$C_{L\alpha}$, $C_{m\alpha}$, $C_{Q\beta}$, …	$\pm 30\,\%$
Mass properties	m, I_{xx}, I_{yy}, I_{zz}	$\pm 10\,\%$
Propulsion	C_T, C_Q	$\pm 15\,\%$

Implementation-related effects are investigated by varying the **transport delays** in the linear closed-loop model. Such delays represent sensor signal transmission, filtering, computation, communica-

tion, and actuator command update effects. Since delays introduce additional phase lag, they can directly reduce the available phase margin and may therefore become critical for fast inner-loop dynamics. The delay analysis is performed by increasing the nominal delay values and recomputing the relevant time- and frequency-domain quantities. This makes it possible to assess how much additional delay can be tolerated before tracking performance deteriorates or robustness margins are violated.

The robustness assessment includes both disk-margin and Nichols-based evaluations. Disk margins are used to quantify simultaneous gain and phase variations at selected loop-breaking points and are therefore suitable for multivariable robustness analysis. In addition, Nichols charts are used as a visual robustness assessment tool. A Nichols diamond defines an exclusion region in the gain-phase plane that must not be penetrated by the open-loop frequency response. The general Nichols plot is depicted in Fig. 7. This representation provides an intuitive visualization of how close the open-loop response is to a critical gain-phase combination. Similar Nichols-diamond constraints are used in [12, 48] to evaluate open-loop robustness at loop cuts in front of the control allocation.

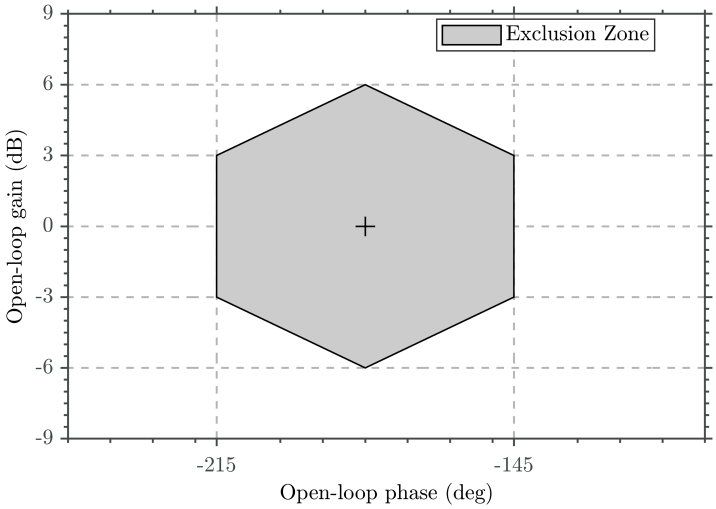


Figure 7 – Nichols plot with exclusive zone according to [48].

The post-optimization linear assessment therefore provides a compact but comprehensive evaluation of the optimized controller. The nominal performance is inspected through step responses and frequency-domain tracking behavior, the robustness properties are evaluated using disk margins and Nichols diagrams, and the sensitivity to modeling errors and implementation delays is analyzed by applying aerodynamic derivative variations, mass and inertia uncertainties, propulsion coefficient variations and additional delay perturbations to the linear closed-loop model.

6 Results

This section presents the results obtained from the linear analysis based on the requirements summarized in Tab. 4 and the optimization workflow described in Section 4. In addition, nonlinear simulations of the optimized EC are performed to assess the behavior outside the linear analysis environment.

The flight controller is implemented with a sampling frequency of 250 Hz, corresponding to a sampling time of 0.004 s. Both the linear and nonlinear systems are evaluated in discrete time. In the linear analysis, the continuous-time model is discretized using the `c2d` command with the `'tustin'` method in MATLAB®. The linear and nonlinear environments include transport delays, as illustrated in Fig. 4. A delay of three samples is considered in the controller command path and an additional delay of three samples is considered in the sensor feedback path. Each path therefore contributes 12 ms of delay, resulting in a combined command-to-feedback delay contribution of 24 ms [49, 50].

6.1 Linear Results

The optimization is performed for hover flight, where the aircraft operates at velocities up to 10 m/s. The gain values obtained from the optimization are listed in Tab. 7.

Table 7 – Gain results of the optimization workflow at the aircraft hover speed.

Gain	Initial	Optimized	Gain	Initial	Optimized	Gain	Initial	Optimized
$K_{P,p}$	2	3.522	$K_{P,\Phi}$	1	1.488	$K_{P,u}$	0.1	0.2898
$K_{P,q}$	2	3.535	$K_{P,\Theta}$	1	1.795	$K_{P,v}$	0.1	0.1531
$K_{P,r}$	2	1.976	$K_{P,\Psi}$	0	0	$K_{P,w}$	0.1	0.1196

The disk-margins obtained from the open-loop cuts introduced in Fig. 6 are summarized in Tab. 8. Only the MIMO disk-margin requirements are used as hard constraints in the optimization. Therefore, g_1 corresponds to the inner-loop disk-margin requirement at $\Delta\nu_{IL}$, while g_2 corresponds to the outer-loop disk-margin requirement at $\Delta\nu_{OL}$.

Table 8 – Disk-margins of the tuned linear system.

Location	GM (dB)	PM (°)	Location	GM (dB)	PM (°)
$\Delta\boldsymbol{\nu}_{IL}$	5.93	36.4	$\Delta\boldsymbol{\nu}_{OL}$	6.88	41.3

The optimized controller satisfies the hard robustness constraints g_1 and g_2, since the MIMO disk-margins exceed the required limits of 3 dB gain margin and 30° phase margin.
For visualization, the inner-loop roll axis is shown in Fig. 8 for command tracking and in Fig. 9 for disturbance rejection. The roll axis is selected because it represents a critical disturbance-rejection case for the considered hover operating point. This selection does not imply that yaw control is generally less demanding in hover. In the present configuration, yaw moments can be generated effectively through propulsion-vectoring effects, whereas lateral wind disturbances directly excite the roll dynamics by acting on the projected side area of the aircraft. The resulting roll moment affects both the roll-rate and roll-angle response.
The tracking results in Fig. 8 show good agreement between the optimized closed-loop response and the desired roll-rate and roll-angle dynamics. The considered parameter uncertainties are introduced at the nonlinear model level. For each of the 500 uncertainty samples, the aircraft is trimmed at the same nominal state condition with varied uncertain parameters. The subsequent linearization yields a corresponding perturbed plant and a local control-effectiveness matrix $\mathbf{B}_\nu$, resulting in 500 different realizations of $\mathbf{B}_\nu$ around the nominal operating point. The controller itself remains fixed at the nominal optimized gain set. The uncertainties have only a minor influence on the response and lead to small deviations from the nominal model. In the time domain, the transport and filter delays introduce a visible response lag and a small overshoot. Nevertheless, the commanded values are reached in steady state and the tracking error converges to zero. In the frequency domain, the peak of the tracking error occurs around 6 rad/s, indicating that the relevant closed-loop bandwidth lies within the intended performance range. The response also remains below the prescribed error weighting, which confirms that the tracking requirement is satisfied.
The disturbance-rejection results are shown in Fig. 9. The time-domain response confirms that the roll-rate and roll-angle errors remain within the prescribed bounds after the disturbance step. The corresponding frequency-domain response supports this observation, since the disturbance transfer remains below the selected error weighting over the relevant frequency range. Under parameter uncertainty, the peak response increases slightly. However, because a sufficient margin to the weighting function remains, the disturbance-rejection requirement is still fulfilled.
The MIMO disk-margins for the inner-loop are shown in Fig. 10. In the presence of uncertainties, the gain and phase margins decrease because the uncertainty samples lead to different local control-effectiveness matrices $\mathbf{B}_\nu$. These variations change the relation between actuator increments and pseudocontrol response. Since the controller is based on the nominal control allocation, deviations between the nominal and sampled effectiveness matrices reduce the available robustness margins. Nevertheless, the disk-margins remain above the required limits, indicating sufficient robustness of the optimized inner loop against the considered uncertainty set.

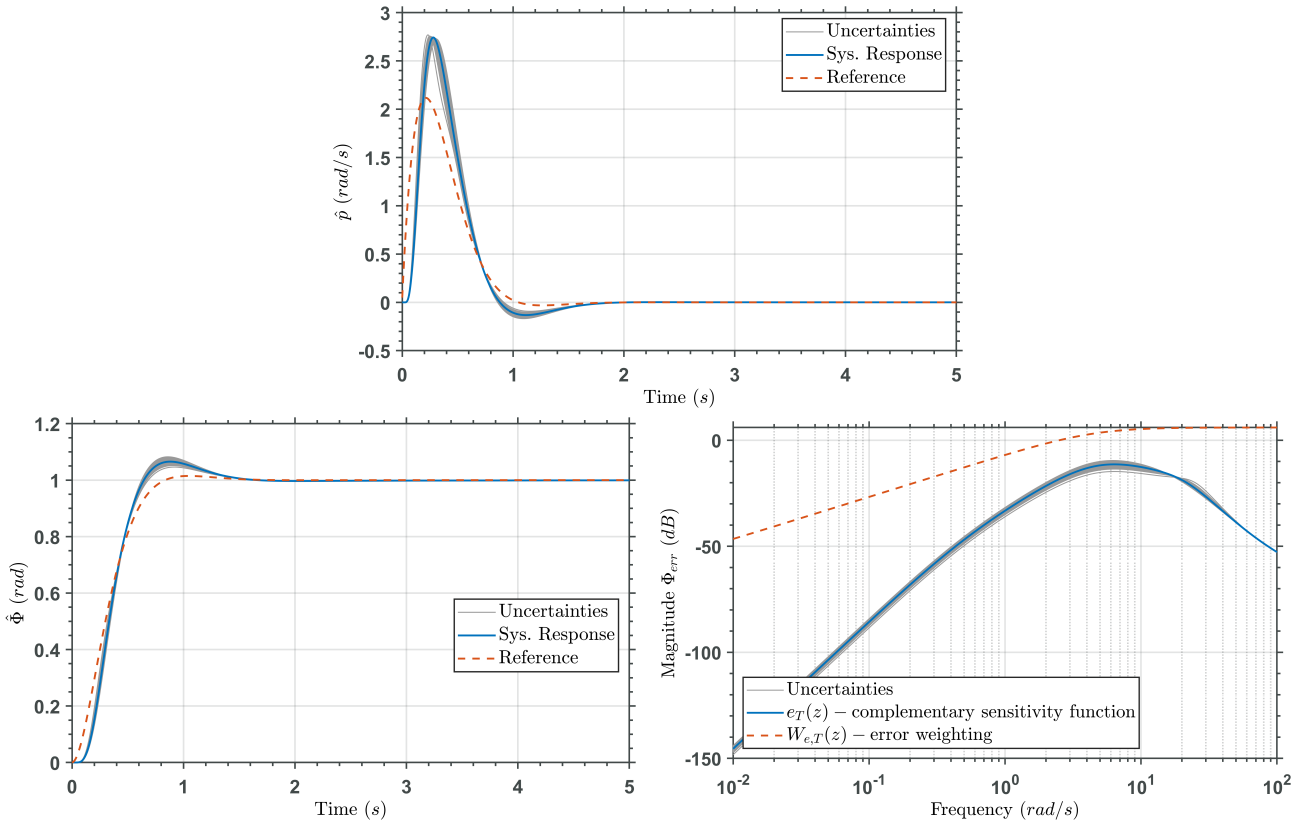


Figure 8 – Tracking performance of the optimized IL in the post-optimization linear assessment.

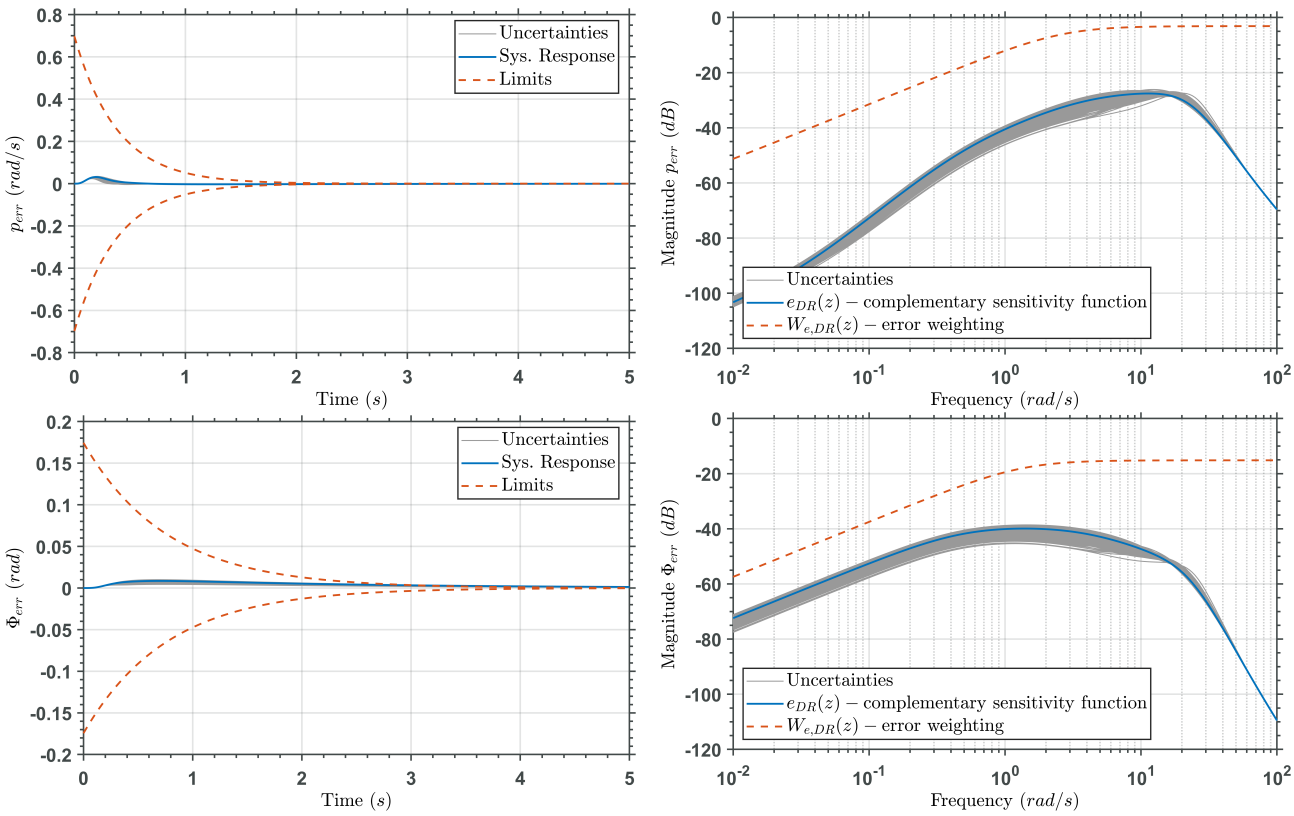


Figure 9 – Disturbance step-rejection performance of the optimized IL in the post-optimization linear assessment.

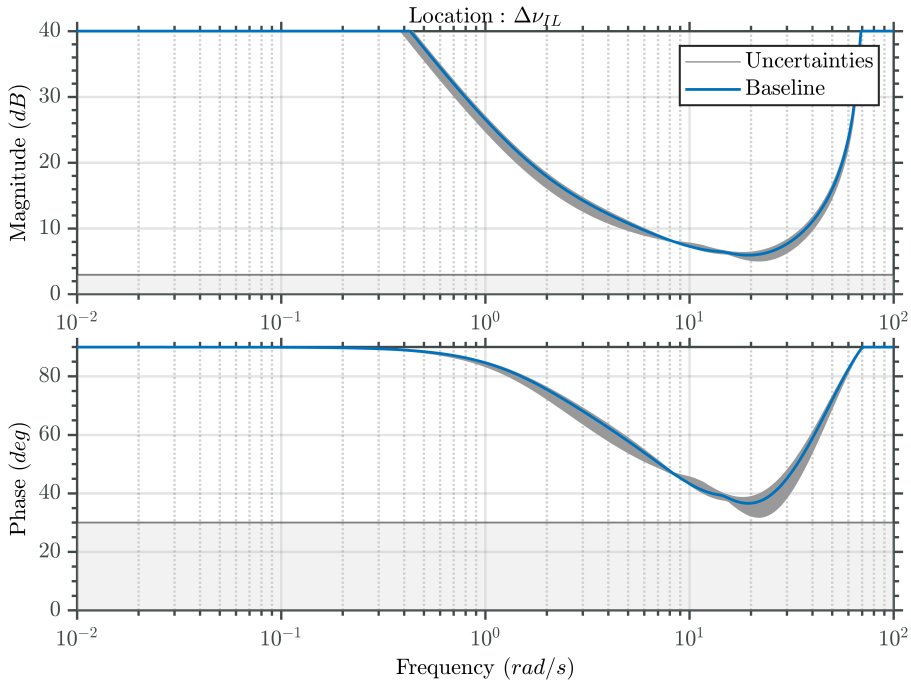


Figure 10 – MIMO disk-margins at $\Delta\boldsymbol{\nu}_{IL}$ for the nominal system and the uncertain model set.

Finally, the influence of additional delays is analyzed using the Nichols chart shown in Fig. 11. As discussed previously, sensor-based INDI control can be sensitive to delays because the incremental control law relies on synchronized actuator, sensor, and derivative information. With the nominal delay of three samples in the command path and three samples in the sensor feedback path, the open-loop responses remain outside the Nichols exclusion region. This indicates that the nominal delayed system retains sufficient robustness. When both the sensor and command delays are increased, the roll and pitch channels enter the exclusion region at approximately 34 samples per path, corresponding to 0.136 s in the command path and 0.136 s in the sensor feedback path. The roll and pitch channels show similar delay sensitivity, whereas the yaw channel remains less affected.

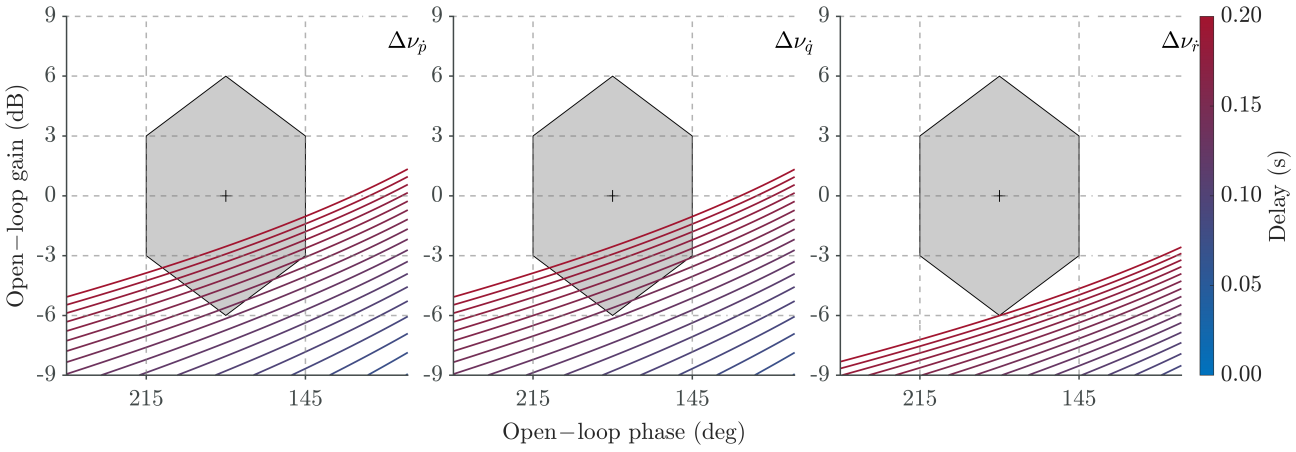


Figure 11 – Nichols chart of the roll, pitch, and yaw channels under increasing delay.

Overall, the linear analysis confirms that the optimized controller satisfies the specified tracking, disturbance-rejection, and robustness requirements in hover flight. The considered parameter uncertainties have a limited influence on the analyzed responses, whereas additional delays have a more pronounced effect on the robustness margins. Nevertheless, the nominal system retains sufficient performance and robustness margins for the considered hover operating condition.

6.2 Nonlinear Simulation

The nonlinear simulation using the controller gains from Tab. 7 is shown for the inner-loop channels in Fig. 12. The simulation represents a hover test case and includes representative sensor behavior, such as noise and nonlinearities, as well as the command and sensor delays considered in the linear analysis. The shown time window contains representative roll, pitch, and yaw-rate commands. The plotted system response is taken from the estimator output and therefore corresponds to the signal available to the EC.

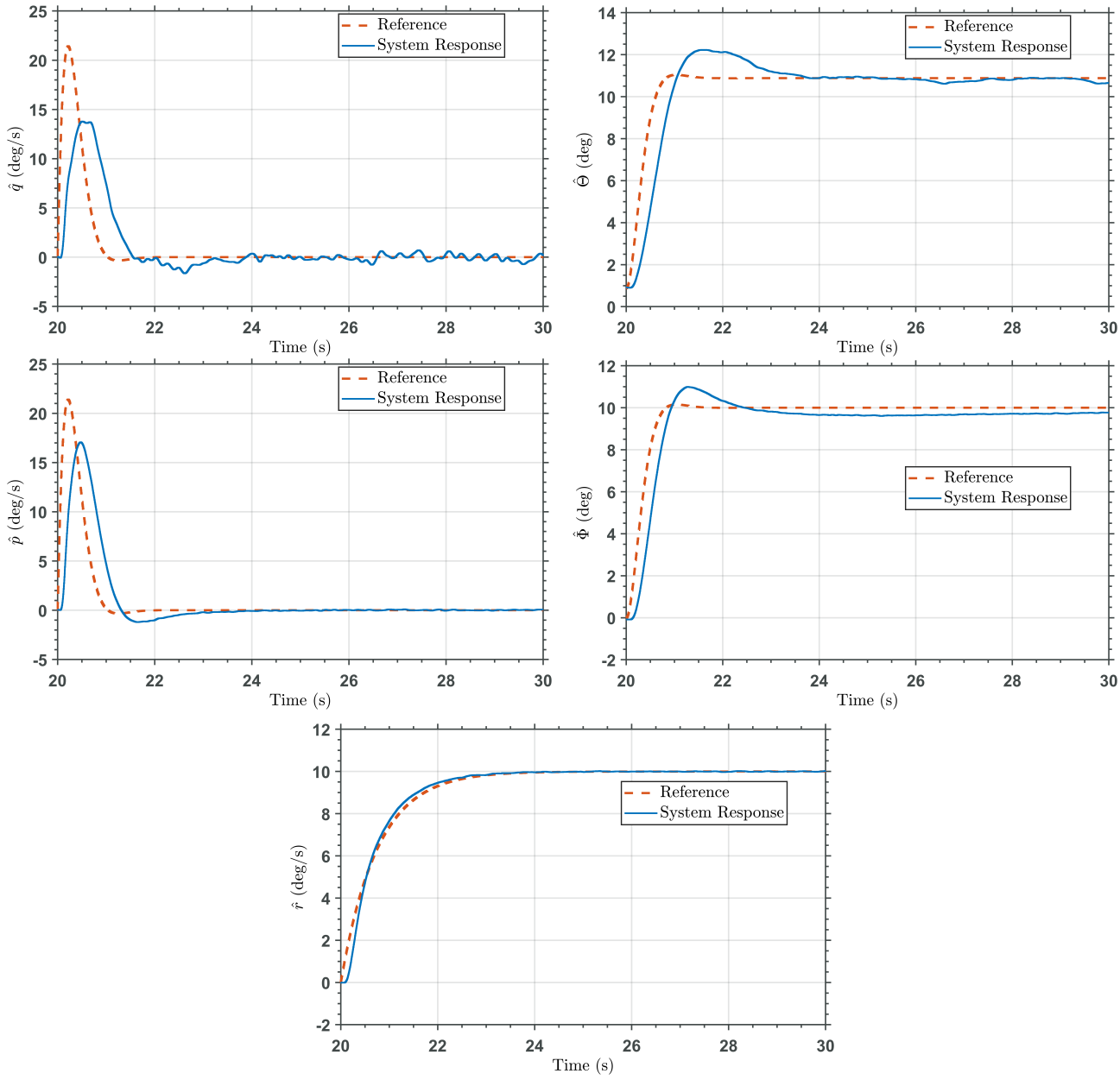


Figure 12 – Closed-loop tracking performance at $0\ m/s$ with sensor errors and delays.

The maneuver consists of roll and pitch attitude commands of 10° and a constant yaw-rate command of $10^\circ/\mathrm{s}$. Overall, the controller tracks the commanded responses well in all inner-loop channels. The roll and pitch attitude responses show a small overshoot, but both converge to the commanded values without a remaining steady-state error. The pitch response reaches its reference faster than the roll response, which is consistent with the different control authority and tuning behavior observed in the linear analysis. The roll- and pitch-rate responses exhibit lower peak values than the corresponding reference-model commands, indicating that the nonlinear closed-loop response is slightly slower than the reference model during the initial transient. Nevertheless, the attitude commands are reached and

the rate errors decay after the maneuver. The yaw-rate channel shows the best agreement with the reference model and reaches the commanded steady-state value with only minor transient deviation. The remaining small oscillations around the steady-state values are mainly caused by the included sensor noise and filtering effects and remain bounded throughout the simulation.

7 Conclusion and Outlook

This paper presented a gain-optimization framework for a cascaded sensor-based INDI controller applied to a fixed-wing eVTOL aircraft. The objective was to formulate the gain-tuning task in a transparent and customizable way by expressing tracking, disturbance-rejection, practical achievability, and robustness requirements as scalar objective or constraint functions. The resulting constrained optimization problem was solved using PSO, while the controller gains were evaluated on a linear closed-loop representation of the aircraft and flight-control system.

The proposed workflow was demonstrated for a hover-flight operating condition of the *PEGASUS* aircraft. The optimized gain set satisfies the prescribed MIMO disk-margin constraints for the inner and outer loops. The linear analysis showed that the optimized controller achieves the required tracking and disturbance-rejection behavior for the selected inner-loop channels. Additional post-optimization analyses were performed to investigate the influence of parameter uncertainties and delays. The uncertainty analysis was based on model perturbations, repeated trimming at the same nominal state condition, and subsequent linearization, resulting in a set of perturbed local control-effectiveness matrices. The results indicate that the considered parameter uncertainties have only a limited influence on the analyzed closed-loop responses, whereas additional command and sensor delays have a more pronounced effect on the robustness margins.

The nonlinear simulation confirms the main findings from the linear analysis for the considered hover test case. The optimized controller tracks roll, pitch, and yaw-rate commands with small deviations and without steady-state error in the attitude channels. The pitch and roll responses show limited overshoot, while the yaw-rate channel follows the reference with the smallest deviation. The remaining small oscillations around the steady-state values remain bounded and are mainly attributed to sensor noise and filtering effects included in the simulation.

The presented results indicate that the proposed optimization workflow can provide a reproducible and requirement-based gain-design process for cascaded sensor-based INDI controllers. Compared with manual tuning, the method allows the tuning objectives and robustness constraints to be stated explicitly. Compared with optimization workflows that rely on nonlinear simulations during each iteration, the linear frequency-domain formulation offers a computationally efficient way to evaluate controller performance and robustness during the gain-search process.

Future work will extend the analysis to additional operating points across hover, transition, and wing-borne flight. This will allow the optimized gains to be scheduled over the flight envelope and evaluated under stronger changes in control effectiveness. Furthermore, the post-optimization uncertainty analysis will be expanded to include larger uncertainty sets and combined perturbations of aerodynamic, propulsion, mass-property, and delay parameters. The nonlinear validation will also be extended to a full aircraft scenario from take-off to landing.

8 Contact Author Email Address

Denis Surmann mailto:denis.surmann@unibw.de
Stephan Myschik mailto:stephan.myschik@unibw.de

9 Copyright Statement

The authors confirm that they, and/or their company or organization, hold copyright on all of the original material included in this paper. The authors also confirm that they have obtained permission, from the copyright holder of any third party material included in this paper, to publish it as part of their paper. The authors confirm that they give permission, or have obtained permission from the copyright holder of this paper, for the publication and distribution of this paper as part of the ICAS proceedings or as individual off-prints from the proceedings.

Declarations

This research, as part of project KISS, is funded by dtec.bw – the Digitalization and Technology Research Center of the Bundeswehr. dtec.bw is funded by the European Union – NextGenerationEU.

References

[1] Anthony Comer, Imon Chakraborty, Yevhenii Kovryzhenko, Ehsan Taheri, Stefanus Putra, Rajan Bhandari, and Bikash Kunwar. Flight Testing of Explicit Model-Following Trajectory Control System for Lift-Plus-Cruise and Tilt-Wing Configurations. *Proceedings of the Vertical Flight Society 80th Annual Forum*, pages 1–26, 0572024.

[2] Thomas Lombaerts, John Kaneshige, Stefan Schuet, Bimal L. Aponso, Kimberlee H. Shish, and Gordon Hardy. Dynamic Inversion based Full Envelope Flight Control for an eVTOL Vehicle using a Unified Framework. *AIAA Scitech 2020 Forum*, 2020.

[3] Pranav Bhardwaj. *Nonlinear Flight Control Strategies for Urban Air Mobility*. PhD thesis, Technical University of Munich, 2024.

[4] Zhidong Lu, Haichao Hong, and Florian Holzapfel. Multi-Phase Vertical Take-Off and Landing Trajectory Optimization with Feasible Initial Guesses. *Aerospace*, 11(1):39, 2024.

[5] Yagiz Kumtepe, Tijmen Pollack, and Erik-Jan van Kampen. Flight Control Law Design using Hybrid Incremental Nonlinear Dynamic Inversion. *AIAA SCITECH 2022 Forum*, 2022.

[6] Agnes Steinert, Stefan Raab, Simon HAFNER, Florian Holzapfel, and Haichao Hong. From fundamentals to applications of incremental nonlinear dynamic inversion: A survey on INDI – Part I. *Chinese Journal of Aeronautics*, 38(11):103553, 2025.

[7] Agnes Steinert, Stefan Raab, Simon HAFNER, Florian Holzapfel, and Haichao Hong. Advancements in incremental nonlinear dynamic inversion and its components: A survey on INDI – Part II. *Chinese Journal of Aeronautics*, 38(11):103591, 2025.

[8] Chong-Sup Kim, Chang-Ho Ji, Gi-Oak Koh, and Byoung Soo Kim. Stability Margin and Structural Coupling Analysis of a Hybrid INDI Control for the Fighter Aircraft. *International Journal of Aeronautical and Space Sciences*, 22(5):1154–1169, 2021.

[9] Stefan Anton Raab. *Contributions to Incremental Nonlinear Dynamic Inversion for Flight Control*. PhD thesis, Technical University of Munich, 2025.

[10] M. Oosterom and R. Babuška. Design of a gain-scheduling mechanism for flight control laws by fuzzy clustering. *Control Engineering Practice*, 14(7):769–781, 2006.

[11] Denis Surmann and Stephan Myschik. Gain Design for an INDI-based Flight Control Algorithm for a Conceptual Lift-to-Cruise Vehicle. *AIAA SCITECH 2024 Forum*, 2024.

[12] Cedric Kotitschke, Tim Rupprecht, Agnes Steinert, Philipp Müller, and Florian Holzapfel. Multiobjective Parameter Optimization of an eVTOL Controller Incorporating Lead-Lag Filters for Increased Robustness. *AIAA AVIATION FORUM AND ASCEND 2024*, 2024.

[13] Anthony M. Comer and Imon Chakraborty. Full Envelope Flight Control System Design and Optimization for a Tilt-Wing Aircraft. *Journal of the American Helicopter Society*, 2024.

[14] Mark Henkenjohann, Udo Nolte, Fabian Sion, Christian Henke, and Ansgar Trächtler. Parameter Tuning Approach for Incremental Nonlinear Dynamic Inversion-Based Flight Controllers. *Actuators*, 13(5):187, 2024.

[15] Denis Surmann, Purav Panchal, and Stephan Myschik. Integrated Flight Control System Architecture and Robustness Analysis for a Lift-to-Cruise Aircraft with Incremental Nonlinear Dynamic Inversion. *Vertical Flight Society 80th Annual Forum & Technology Display*, pages 1–14, 2024.

[16] Brian L. Stevens, Frank L. Lewis, and Eric N. Johnson. *Aircraft control and simulation: Dynamics, controls design, and autonomous systems*. Wiley, Hoboken, New Jersey, 3. ed. edition, 2016.

[17] Rudolf Brockhaus, Wolfgang Alles, and Robert Luckner. *Flugregelung*. Springer, Berlin, Heidelberg, 2011.

[18] Wayne Durham. *Aircraft Flight Dynamics and Control*. New York Academy of Sciences Series. John Wiley & Sons Incorporated, Newark, 1st ed. edition, 2013.

[19] Quan Quan. *Introduction to Multicopter Design and Control*. Springer Singapore, Singapore, 2017.

[20] Florian Schwaiger, Chinmaya Mishra, and Florian Holzapfel. Acceleration Framework to Quantify the Influence of Uncertain Parameters on Simulation Models using Matlab and Simulink. *AIAA Scitech 2021 Forum*, 2021.

[21] Florian Holzapfel. *Nichtlineare adaptive Regelung eines unbemannten Fluggerätes*. PhD thesis, Technical University Munich, Munich, 2004.

[22] P. Smith. A simplified approach to nonlinear dynamic inversion based flight control. *23rd Atmospheric Flight Mechanics Conference*, 1998.

[23] Barton Bacon and Aaron Ostroff. Reconfigurable flight control using nonlinear dynamic inversion with a special accelerometer implementation. *AIAA Guidance, Navigation, and Control Conference and Exhibit*, 2000.

[24] S. Sieberling, Q. P. Chu, and J. A. Mulder. Robust Flight Control Using Incremental Nonlinear Dynamic Inversion and Angular Acceleration Prediction. *Journal of Guidance, Control, and Dynamics*, 33(6):1732–1742, 2010.

[25] Xuerui Wang, Erik-Jan van Kampen, Qiping Chu, and Peng Lu. Stability Analysis for Incremental Nonlinear Dynamic Inversion Control. *Journal of Guidance, Control, and Dynamics*, 42(5):1116–1129, 2019.

[26] Pranav Bhardwaj, Stefan A. Raab, Jiannan Zhang, and Florian Holzapfel. Integrated Reference Model for a Tilt-rotor Vertical Take-off and Landing Transition UAV. *2018 Applied Aerodynamics Conference*, 2018.

[27] Jean-Jacques E. Slotine and Weiping Li. *Applied nonlinear control*. Prentice Hall, Englewood Cliffs, NJ, 1991.

[28] Rasmus Steffensen, Agnes Steinert, Zoe Mbikayi, Stefan Raab, Jorg Angelov, and Florian Holzapfel. Filter and sensor delay synchronization in incremental flight control laws. *Aerospace Systems*, 2023.

[29] Sigurd Skogestad and Ian Postlethwaite. *Multivariable feedback control: Analysis and design*. Wiley, Chichester, 2. ed., repr edition, 2010.

[30] R. Eberhart and J. Kennedy. A new optimizer using particle swarm theory. *MHS'95. Proceedings of the Sixth International Symposium on Micro Machine and Human Science*, pages 39–43, 1995.

[31] J. Kennedy and R. Eberhart. Particle swarm optimization. *Proceedings of ICNN'95 - International Conference on Neural Networks*, pages 1942–1948, 1995.

[32] Kalyanmoy Deb. An efficient constraint handling method for genetic algorithms. *Computer Methods in Applied Mechanics and Engineering*, 186(2-4):311–338, 2000.

[33] Jan Lunze. *Regelungstechnik 2*. Springer Berlin Heidelberg, Berlin, Heidelberg, 2010.

[34] P. Apkarian and D. Noll. Nonsmooth H_∞ Synthesis. *IEEE Transactions on Automatic Control*, 51(1):71–86, 2006.

[35] P. Apkarian, D. Noll, and A. Rondepierre. Mixed H_2/H_∞ Control via Nonsmooth Optimization. *SIAM Journal on Control and Optimization*, 47(3):1516–1546, 2008.

[36] Da-Wei Gu, Petko Hr. Petkov, and M. M. Konstantinov. *Robust control design with MATLAB®*. Advanced Textbooks in Control and Signal Processing. Springer, London and Heidelberg, 2. ed. edition, 2013.

[37] Keith Glover. Multiplicative approximation of linear multivariable systems with L ∞ error bounds. *1986 American Control Conference*, pages 1705–1709, 1986.

[38] Peter Seiler, Andrew Packard, and Pascal Gahinet. An Introduction to Disk Margins [Lecture Notes]. *IEEE Control Systems*, 40(5):78–95, 2020.

[39] JAMES D. BLIGHT, R. LANE DAILEY, and DAGFINN GANGSAAS. Practical control law design for aircraft using multivariable techniques. *International Journal of Control*, 59(1):93–137, 1994.

[40] Fabian Grondman, Gertjan Looye, Richard O. Kuchar, Q. Ping Chu, and Erik-Jan van Kampen. Design and Flight Testing of Incremental Nonlinear Dynamic Inversion-based Control Laws for a Passenger Aircraft. *2018 AIAA Guidance, Navigation, and Control Conference*, 2018.

[41] Gertjan Looye and Hans-Dieter Joos. Design of robust dynamic inversion control laws using multi-objective optimization. *AIAA Guidance, Navigation, and Control Conference and Exhibit*, 2001.

[42] João T. Diz, Spilios Theodoulis, and Pedro Simplício. Thrust Vector Control for Flexible Launch Vehicles: An H-Infinity Open Loop Shaping Approach. *AIAA SCITECH 2026 Forum*, 2026.

[43] Lorenzo Favaro, Agata Rylko, and Giuseppe Quaranta. Building Credible VTOL Flight Models for Handling Quality Certification by Simulation. *Aerospace*, 12(6):559, 2025.

[44] Andreas Hövelmann and Christian Breitsamter. Aerodynamic Characteristics of the SAGITTA Diamond Wing Demonstrator Configuration. *Deutscher Luft- und Raumfahrtkongress 2012*, 2012.

[45] Huascar Mirko Montecinos Cortez, Neusa Maria Franco de Oliveira, and Francisco Javier Triveno Vargas. INDI control for the take-off and landing phases of an eVTOL. *International Journal of Dynamics and Control*, 14(6), 2026.

[46] Erlend M. Coates, Andreas Wenz, Kristoffer Gryte, and Tor Arne Johansen. Propulsion System Modeling for Small Fixed-Wing UAVs. *2019 International Conference on Unmanned Aircraft Systems (ICUAS)*, pages 748–757, 2019.

[47] Hairuniza Kutty and Parvathy Rajendran. 3D CFD Simulation and Experimental Validation of Small APC Slow Flyer Propeller Blade. *Aerospace*, 4(1):10, 2017.

[48] David Rainer Seiferth. *Flight Control Function Enhancements For Novel Aerial Vehicles*. PhD thesis, Technical University Munich, Munich, 2022.

[49] Zhuoqun Cheng, Richard West, and Craig Einstein. End-to-End Analysis and Design of a Drone Flight Controller. *IEEE Transactions on Computer-Aided Design of Integrated Circuits and Systems*, 37(11):2404–2415, 2018.

[50] PX4 Development Team. MC Filter Tuning & Control Latency, 2026.